

Linköping Studies in Science and Technology

Dissertation No. 1153

Nanocrystalline Alumina-Zirconia Thin Films Grown by Magnetron Sputtering

David Huy Trinh



Linköping University
INSTITUTE OF TECHNOLOGY

Thin Film Physics Division

Department of Physics, Chemistry and Biology (IFM)

Linköpings universitet, SE-581 83 Linköping, Sweden

2008

Cover image

Alumina-zirconia coated silicon wafers mounted on a stage awaiting x-ray photoelectron spectroscopy measurements.

The different colours result as the films are of different thicknesses in the region ($<1 \mu\text{m}$) where the light reflecting off the film/substrate interface constructively interferes with light reflecting off the film surface. As the thickness of the films vary, the wavelength of light that constructively interferes will change and hence the different colours. This effect, while interesting physics, is only tangential to the ideas promoted in this thesis.

© David Huy Trinh, 2008

ISBN: 978-91-85895-18-2

ISSN: 0345-7524

Printed by LiU-Tryck, Linköping, Sweden

“But what is the point of dawn now,
when one can read outside without it?”

I challenge you all now, all of you atheists:
how are you going to save the world
and where have you found the right road for it –
you men of science, industry, associations, wages and the like? How?
With credit? What is credit? Where will credit take you?

Yes, but the universal need to live, drink and eat,
and the most complete, indeed scientific conviction,
that one cannot satisfy need without universal association and
a solidarity of interests, is,
I think, an idea of strong enough to serve as a point of support and
a “spring of life” for future ages of mankind”

Gavrila Ardalionovich in *The Idiot* by Fyodor Dostoyevsky

Abstract

Alumina-zirconia thin films have been deposited using dual magnetron sputtering. Film growth was performed at relatively low-to-medium temperatures, ranging from $\sim 300^{\circ}\text{C}$ to 810°C . Different substrates were applied, including silicon (100), and industrially relevant materials, such as WC-Co hardmetal. Both radio-frequency sputtering and direct-current magnetron sputtering were utilised to achieve a range of film compositions. The influence of sputtering target was investigated; both ceramics and metals were used as sources. Microstructural characterisation was performed with a range of electron microscopy and x-ray diffraction techniques which show that the pure zirconia was deposited in the monoclinic phase. Reduced mobility of depositing species, as in the case of direct-current sputtering, yielded preferred crystallographic orientation in the $\{100\}$ directions. The initial nucleation layer consisted of the metastable tetragonal zirconia phase. This phase could be grown over film thicknesses $\sim 1\ \mu\text{m}$ through the addition of $\sim 3\ \text{at.}\%$ Al under similar low mobility conditions. For cases of higher mobility, as obtained through radio-frequency sputtering, the metastable cubic zirconia phase formed in the film bulk for alumina-zirconia nanocomposites. A combination of two mechanisms is suggested for the stabilisation of metastable zirconia phases: oxygen-deficiency and aluminium segregations with resultant restraint on the zirconia lattice. The sputter deposition process was investigated through energy resolved mass spectrometry in the case of radio-frequency RF sputtering; the sputter deposition flux contained a mixture of metallic ions, metal-oxygen clusters, and oxygen ions. The presence of metal-oxygen clusters was found to be important in oxygen-stoichiometry and thus the phase selection of the resultant film. The energy distributions were similar when comparing sputtering from ceramic and metallic targets. A mass-balance model has also been developed for the transport phenomena and reactions of particles in reactive sputtering of two targets in a two-gas scenario for the alumina-zirconia system. Addition of nitrogen to the working gas was found to eliminate the hysteresis in the target poisoning for oxygen reactive sputtering. The higher reactivity of oxygen contributed to a higher oxygen content in resultant films compared to the oxygen content in the oxy-nitride working gas. The model was thus shown to be successful for tuning depositions in the alumina-zirconia oxy-nitride system.

Preface

“Once more unto the breach, dear friends, once more;”
William Shakespeare: *Henry V*

This doctorate thesis concerns the growth and characterisation of alumina-zirconia nanocomposites. It is a collaborative effort between Linköpings universitet and Sandvik Tooling AB. The research has also been supported through the Swedish Research Council (VR) and the Swedish Foundation for Strategic Research (SSF) Strategic Research Centre on Materials Science for Nanoscale Surface Engineering (MS²E).

Publications in this thesis

Paper 1

“Radio frequency dual magnetron sputtering deposition and characterization of nanocomposite Al₂O₃-ZrO₂ thin films” D.H. Trinh, H. Högberg, J.M. Andersson, M. Collin, I. Reineck, U. Helmersson and L. Hultman, *Journal of Vacuum Science and Technology A* **24** (2006) 309

Synthesis, characterisation, analysis and manuscript preparation were performed by the first author with assistance of others.

Paper 2

“Nanocomposite Al₂O₃-ZrO₂ thin films grown by reactive dual radio-frequency magnetron sputtering” D.H. Trinh, M. Ottosson, M. Collin, I. Reineck, L. Hultman and H. Högberg, *Thin Solid Films* (In press)

Synthesis, characterisation, analysis and manuscript preparation were performed by the first author with assistance of others. Supporting x-ray diffraction and ion beam experiments including data analysis were performed by co-authors.

Paper 3

“DC magnetron sputtering deposition of nanocomposite alumina-zirconia thin films” D.H. Trinh, T. Kubart, T. Nyberg, M. Ottosson, L. Hultman, H. Högberg (Submitted)

Synthesis, characterisation, analysis and manuscript preparation were performed by the first author with assistance of others. Supporting x-ray diffraction and spectroscopy including data analysis were performed by co-authors and assisting technical staff.

Paper 4

“Experiments and Modelling of Dual Reactive Magnetron Sputtering using two Reactive Gases” T. Kubart, D.H. Trinh, L. Liljeholm, L. Hultman, H. Högberg, T. Nyberg, S. Berg (Submitted)

Experiments, modelling, analysis and manuscript preparation were performed in Uppsala by the first author with assistance of the co-authors.

Paper 5

“Mass-spectrometry of the positive-ion flux during radio-frequency sputter deposition of alumina-zirconia nanocomposites” D.H. Trinh, L. Hultman and H. Högberg, (Manuscript in final preparation)

Measurements, analysis and manuscript preparation were performed by the first author with the assistance of the co-authors.

Related publications not included in the thesis

“Influence of the normalized ion flux on the constitution of alumina films deposited by plasma assisted chemical vapour deposition” D. Kuraprov, J. Reiss, D.H. Trinh, L. Hultman, J.M. Schneider *Journal of Vacuum Science and Technology A* **25** [4] (2007) 831

“Towards an understanding of the machining properties of κ - and γ -Al₂O₃ coated cutting inserts” D.H. Trinh, K. Back, H. Blomqvist, G. Pozina, T. Selinder, M. Collin, I. Reineck, L. Hultman, H. Högberg (Manuscript in final preparation)

“Coated insert” D.H. Trinh, H. Högberg, L. Hultman, M. Collin, I. Reineck, Swedish Patent SE-0600104-4 (European Patent EP1717347)

Acknowledgements

“At times our own light goes out and is rekindled by a spark from another person. Each of us has cause to think with deep gratitude of those who have lighted the flame within us.”
Albert Schweiter

My four supervisors: **Hans Högborg**, while you keep repeating the fact that I have driven myself through my PhD, I am still grateful that you are there occasionally to stop me driving into a tree. **Marianne Collin**, for the friendly guidance and for always asking questions when we are both confused. **Lars Hultman** and **Ingrid Reineck**, for their steady strategic guidance during the project, especially when short on time.

Technicians: **Thomas Lingefelt**, **Kalle Brolin** and **Masanori Mori** who would easily out-MacGyver MacGyver. **Inger Eriksson**, for all the administrative help.

My mentor: **Mats Sundberg**, for providing a ball plank to bounce ideas off and for all the advice, coffee, tea and lunches.

I have had the wonderful opportunity to travel around the world to perform analyses or at least send my samples around the world to have analysis performed. As such, there is a long list of people who have contributed to the process of collecting data in this thesis as well as many long scientific discussions.

- o Sandvik Tooling, Sweden – **Torbjörn Selinder**, **Alexandra Kusoffsky**, **Helena Blomqvist**, **Susanne Norgren**, **Cecilia Århammar**
- o Uppsala University, Sweden – **The Tomas Twins: Nyberg and Kubart**, **Mikael Ottosson**, **Lina Liljeholm**, **David Martin**
- o RWTH Aachen, Germany – **Jochen Schneider**, **Jennifer Reiß**, **Stanislav Mráz**
- o ONERA Châtillon, France – **Gilles Hug**, **Noël Haddad**
- o FZR Rossendorf, Germany – **Ulli Kressig**
- o Montanuniversität Leoben, Austria – **Herbert Willmann**
- o Drexel University, USA – **Jonathan Spanier** and **Stephen Nonnemann**

An equally long list would be all my colleagues at the **Thinfilm Physics** division, now accompanied by the **Plasma and Coating Physics** and **Nanostructured Materials**, divisions. Thank you to all those who have had the patience to show me how to use equipment, tried to teach me new things or teach me old things which I simply don't understand, or have endured my inquisition-like questioning. It has been an absolute pleasure working at work, being distracted at work and on the various distractions away from work.

My friends, I am sure you all know who you are, there is much to thank you for: listening to my constant complaints, providing interesting points of discussion, convincing me to join lindy hop cult, the beer and wine, challenging me in swimming or squash, eaten my attempts at cooking. All these “side” activities keep me sane.

My family, near and extended for all the telephone time, the support and all the food and **李嘉茵** for all the time, the support and for reminding me to “think positive”.

Table of Contents

Introduction	- 1 -
Objectives	- 2 -
Outline	- 2 -
The Alumina-Zirconia Material System.....	- 3 -
Zirconia.....	- 3 -
Monoclinic Zirconia	- 3 -
Alumina	- 5 -
Alumina-Zirconia	- 7 -
Plasmas and Sputtering	- 11 -
Plasma Basics.....	- 11 -
Sputtering	- 13 -
Reactive Sputtering	- 17 -
Capacitive Plasmas – Radio-Frequency	- 23 -
Characterising Plasmas	- 26 -
Thin Film Growth.....	- 29 -
Novel Structures.....	- 29 -
Structural Morphology.....	- 31 -
Crystallographic Effects	- 32 -
Analysis Techniques.....	- 35 -
X-Ray Diffraction.....	- 35 -
Transmission Electron Microscopy	- 39 -
Ion Beam Techniques	- 51 -
X-Ray Photoelectron Spectroscopy.....	- 53 -
Summary and Contribution to the Field	- 57 -
Future Outlook.....	- 59 -
References	- 61 -
Populärvetenskaplig sammanfattning	- 67 -
(Popular Science Description in Swedish)	
Papers 1 – 5	- 69 -

Introduction

“And what if – without waiting – I plunge myself head down?
Would it not be the only, the correct way – disentangling everything at once?”
Yevgeny Zamyatin: *We*

Oxide ceramics have been well established as having a good combination of mechanical properties and oxidation resistance. They are thus, often used in demanding high-temperature environments [1]. Alumina and zirconia are typical examples of such oxide structural ceramics. Recently, there has been increasing interest in alumina-zirconia thin films for a number of applications; these include wear resistant coatings [2], diffusion barriers [3], thermal barrier coatings [4] and dielectric coatings [5]. The interest in thin films has arisen as novel structures can be achieved by techniques that operate far from equilibrium, such as vapour techniques [6]. For the alumina-zirconia system, this is particularly the case as both pure oxide systems contain a multitude of metastable phases that can be beneficial in various applications [7,8] and which have properties that vary significantly from the thermodynamically stable phases. The wide range of possible structures means that the properties of a film can be designed according to nature and proportion of phases present in a particular film structure. In order to achieve these metastable phases, non-equilibrium growth techniques must be employed.

Magnetron sputtering is a well established thin film growth technique that offers a compromise between depositing at an atomic level and reasonable deposition rates. This method also allows deposition at relatively low temperatures, which is valuable in the synthesis of novel structures containing metastable, non-equilibrium phases or of highly oriented materials. The process is, however, rather complex with many variables affecting the final coating. There is a need not only for the development of new coatings but also for investigation of how the synthesis process affects the final properties of a film.

Growth of pure alumina by sputtering has posed numerous problems in terms of achieving crystalline films, which has traditionally required temperatures >500 °C [9], and in terms of achieving a stable process that provides for high growth rate [10]. Growth of pure zirconia thin films is comparatively easier, with larger process

windows and many reports of crystalline films sputtered at low substrate temperature [11 – 14]. Sputter deposition of mixed alumina-zirconia thin films remains, however, dominated by the same challenges of depositing pure alumina films by sputtering. As a result, alumina-zirconia thin films produced by sputtering have often employed special micro and nanostructures, such as multilayers [15,16], or required annealing at temperatures > 1000 °C [17,18] in order to form crystalline films. In addition, the understanding of the mechanisms that underlie the formation of crystalline phases in the sputtering process must also be investigated. Hence the plasma and its interaction to the sputter system are also of interest.

Objectives

The aims of this work are, first, to synthesise nanocomposite oxide thin films with novel structures; alumina-zirconia nanocomposites were chosen due to their wide range of potential applications. Secondly, having achieved these new structures, characterisation of the resultant micro- and nanostructure must be performed. Finally, the growth mechanisms behind the formation of these films must be studied. To this end, the sputtering plasma, particularly the particles within the plasma and the transport phenomenon of these particles, has been studied.

Outline

In this thesis the alumina-zirconia material system is first presented. Following this, the growth process of sputter deposition and mechanisms of thin film growth are examined. The methods used to characterise the films are then catalogued followed by a summary of the major results obtained and the future outlook of such work. The results themselves are presented in the form of the five included papers, of which **Papers 1 – 3** focus on the growth of novel micro- and nanostructures and characterisation of such structures, while **Papers 4 and 5** focus on understanding the sputter deposition process and the actual mechanism of growth of the structures presented in the former papers.

The Alumina-Zirconia Material System

“The realities of nature surpass our most ambitious dreams.”
Francois Rodin

Zirconia

Zirconia in bulk form is well known for high temperature stability and corrosion resistance [19]. Indeed, zirconia is used in the harsh conditions of glass making and steel casting [20]. As a thin film coating, zirconia has been applied as thermal barrier coatings where high temperature stability and corrosion resistance are critical [21]. Zirconia has been studied as bulk material extensively due to the tetragonal to monoclinic phase transformation and the associated metastable structures [22]. This transformation has led to zirconia being referred to as “ceramic steel” [23]. There are three main phases of interest in the equilibrium phase diagram [22,24]: the monoclinic, tetragonal and cubic phases, seen below in Figure 1.

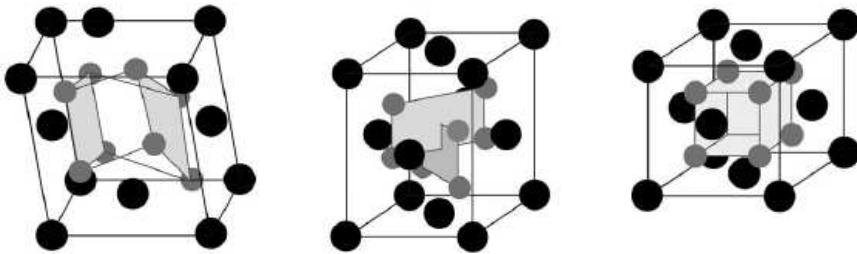


Figure 1: The main phases of interest in zirconia:

Monoclinic [25,26] (left), tetragonal (centre) and cubic (right) [22,25,26].

Anions marked in grey, cations marked in black.

Monoclinic Zirconia

This is the thermodynamically stable phase at room temperature and, as such, is generally the final phase after the transformation of metastable phases. The structure belongs to the $P2_1/c$ space group [8]. The Zr^{4+} ion has a seven-fold coordination, while the oxygen atoms are nearly tetrahedral, one angle deviating significantly from the tetrahedral angle. This phase is the largest of the equilibrium phases by volume [22,27]. Under equilibrium conditions, this phase is stable up to 1170 °C, upon which it transforms to the tetragonal phase. The monoclinic phase was the primary phase

formed when pure zirconia was deposited in **Papers 1 – 3**. This phase remained stable upon addition of small amounts, ~1 at.%, of aluminium, but upon further addition of aluminium, other phases formed. None of the films produced in this study resulted in phase pure monoclinic zirconia and this phase always coexisted with other zirconia phases.

Tetragonal zirconia

The tetragonal phase belongs to the $P4_2/nmc$ space group and is typically stable at temperatures between 1170 °C and 2370 °C under equilibrium conditions [8]. The Zr^{4+} ion has an eight-fold coordination, while the oxygen ions are split evenly into two types: those coordinated as a flattened tetrahedron and those as an elongated tetrahedron. The volume of the tetragonal phase is smaller than that of the monoclinic phase, leading to a 4% volume expansion upon transformation to the monoclinic phase. The tetragonal phase is typically stabilised at room temperature in bulk ceramics through the addition of other oxides such as yttria, ceria or magnesia [28], stabilisation is also possible in alumina-zirconia nanocomposites when the grain-size reduces below 1 μm [29,30]. This was the case in **Paper 3** where ~3 at.% aluminium was sufficient to stabilise the tetragonal phase. Size effects have long been known to influence the formation of tetragonal zirconia, even without additions of other elements [23]. It has been suggested that the stabilisation is due to the lower surface energy of the tetragonal phase compared to the monoclinic phase [31], although there is some conjecture as to whether this is actually the case [32]. Additional stabilising effects have also been suggested in **Paper 3**, where the tetragonal zirconia formed as an initial nucleation layer prior to the formation of the thermodynamically stable monoclinic phase.

Cubic zirconia

The cubic phase is the high-temperature phase of zirconia and is typically present from 2370 °C to the melting temperature 2680 °C [8]. The structure belongs to the $Fm\bar{3}m$ space group based on the fluorite structure, a face-centred cubic structure [24,26]; each Zr^{4+} ion has eight-fold coordination, while each oxygen ion is tetrahedrally coordinated and form a simple cubic sub-lattice. The cubic phase has an even smaller volume than the tetragonal phase of zirconia and is attained at room temperature by the addition of stabilisers, in greater quantity than that required for the

tetragonal phase [22]. The cubic phase is the only phase of the equilibrium phases with a sizeable oxygen homogeneity region at room temperature, ranging from 61 at.% to 66.6 at.% [24]. This oxygen deficiency has been observed previously in thin films [33] and it is suggested that this mechanism is responsible for the formation of the cubic zirconia phase in **Paper 1**. Another mechanism must, however, exist since the formation of a similar cubic phase in **Paper 2** was found in a situation where an abundance of oxygen in the plasma existed.

Other metastable phases

Many metastable phases exist outside the three main phases, some of which are distortions of the tetragonal or the cubic phases [34,35]. Indeed, the tetragonal phase can be considered as a distortion of the cubic phase. The difference arises by simply shifting oxygen columns alternatively up and down in the [001] directions [26]. This shift leads to new periodicity in the (112) plane. Other distortions are often marked t' or t'' . These phases are common in coating processes, such as plasma spraying, which deposit material far from equilibrium conditions [4]. There also exists an orthorhombic phase and a cotunnite structure, typically associated with high pressures [26,36].

Alumina

Alumina is one of the most studied ceramics due to a favourable combination of physical, chemical, mechanical and thermal properties [7]. Alumina is used in refractories, hard coatings, electrical applications and glass-making, just to take a small selection of the possible applications. This versatility arises from the many different forms in which alumina can be produced. The most commonly studied form is the α -phase, commonly known as corundum. This is the thermodynamically stable phase of alumina at atmospheric temperature and pressure, remaining stable up to the melting point [24]. There exist many metastable phases that are also commonly synthesised, allowing alumina containing materials to be tailored to specific applications, although obtaining a particular desired alumina phase or structure may be quite difficult. Metastable phases of interest in thin films include κ -, γ - and θ -alumina. The oxygen sub-lattice is close-packed in all phases of alumina, with only slight distortions between the various phases, see Figure 2.

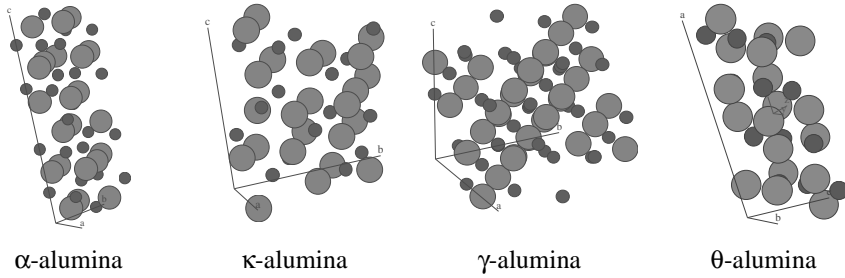


Figure 2: Alumina phases of interest in thin films [37 – 39]

α -alumina

The pure, room-temperature phase of alumina is both transparent and uncoloured. This phase is trigonal, belonging to the space group $R\bar{3}c$ and has two *formula units* (10 atoms) in the primitive unit cell [40]. It is more commonly represented as a hexagonal structure [39] with six *formula units* in each unit cell and has also been referred to as being in the rhombohedral system [7,41]. The oxygen sub-lattice is represented by hexagonal close-packed structure with the aluminium atoms occupying two thirds of the octahedral interstitial sites and features ABAB stacking [7,42]. No stable condensed phase exists that is richer in oxygen than the α -alumina phase [24].

κ -alumina

The κ -alumina phase is a metastable phase that is common for wear-resistant coatings produced by chemical vapour deposition. The phase features an orthorhombic structure with octahedrally and tetrahedrally coordinated aluminium ions, the stacking in the structure is ABAC [43]. This phase belongs to the $Pna2_1$ space group [44]. The κ -alumina phase is less dense and a volume contraction is associated with the transformation to the stable α -alumina phase commonly causing cracking upon cooling [45].

γ -alumina

Common in films deposited through sputtering, γ -alumina remains somewhat a mystery with some debate to the actual structure. It has been represented as a cubic, defect-spinel structure in the $Fd\bar{3}m$ space group [37,39,46], but also as a tetragonal structure [47]. In the former case, which is more frequent, the structure can be described with one single cubic close-packed anion sub-lattice and two cation sub-

lattices, one containing octahedral sites and the other containing tetrahedral sites [48]. Alternatively, γ -alumina can be described as six repeating non-equivalent (111) planes of either Al or O atoms based on a hexagonal arrangement of O atoms with 2.80 Å spacing [49]. It should be noted that the structure does contain some partial disorder in the ions [50], since aluminium does not fully occupy all the available cation sites [48]. There has been considerable interest in the γ -alumina structure recently for wear resistant thin-film coatings and as a catalytic surface [51 – 55]. A major advantage of the γ -alumina coatings has been the ability to produce this structure at considerably lower temperatures than required to produce crystalline alumina films of the κ and α phases. The γ -alumina phase is also stable up to temperatures of 750 °C [56]. This phase was deposited in the case of pure alumina in **Paper 2**. Given the low deposition temperatures and the thermodynamics of mixing, the films containing alumina in the other papers were generally amorphous.

θ -alumina

θ -alumina is monoclinic belonging to the $C2/m$ space group [37]. This phase has been suggested as an intermediate phase for transformations from γ to α particularly in bulk materials [39,57,58]. Phase-mixed alumina coatings containing the θ -alumina phase have also been produced with ionized magnetron sputtering at low temperatures [59]. This structure is considerable less dense than the α phase.

Alumina-Zirconia

Binary phase diagram

Pure alumina or pure zirconia are both ceramic materials and, as such, are inherently brittle. It is possible to toughen these materials through the addition of a second phase [60], hence the motivation for the development of alumina-zirconia composites. Upon mixing alumina and zirconia, a number of metastable phases may form, such as the aforementioned tetragonal or cubic zirconias [8,61] and the γ -alumina phase [52]. The alumina-zirconia quasi-binary system in Figure 3 is characterised by little solubility between the equilibrium phases at room temperature or higher temperatures up to the eutectic point [61,62]. A eutectic is formed at 1866 °C [63] and naturally there is greater solid solubility at this temperature (8 at.% \pm 2 at.% Al_2O_3 in ZrO_2 and

3 at.% \pm 2 at.% ZrO_2 in Al_2O_3). Most composites are thus likely to form phase-separated microstructures unless supersaturation occurs. The presence of alumina has been shown to affect the transformation of the tetragonal zirconia phase in the bulk form [30] and in the thin film form [15,16]. The solubility of individual solute atoms, such as aluminium in zirconia or zirconium in alumina, should also be considered given the nature of thin film growth. The cubic zirconia phase has the most tolerance for the aluminium atom, at 2 at.% solubility [8]. The tetragonal zirconia phase features little solubility. It should however be noted that in cases of extreme oxygen deficiency, the alumina-zirconia quasi-binary phase diagram is no longer valid and as such aluminium-zirconium ordered phases are possible [64].

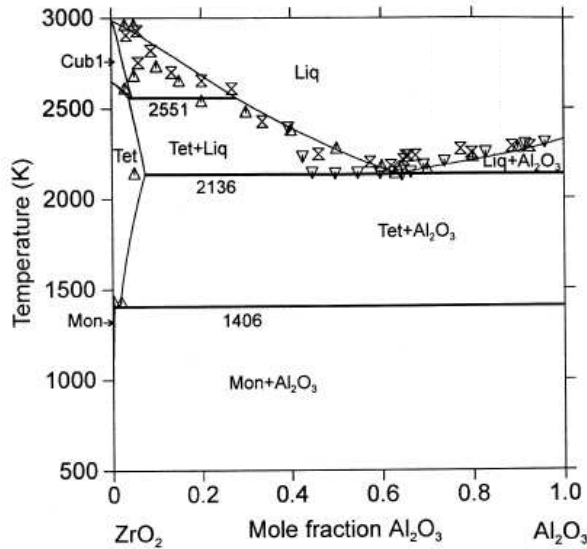


Figure 3: Alumina-zirconia quasi-binary phase diagram [62]

Material toughening in composites

The phase separation into distinct alumina and zirconia phases has been used extensively to toughen the ceramic materials. There are a variety of mechanisms outside the phase transformation in zirconia that make ceramic composites tougher than ordinary pure single oxide phase counterparts. A short review of toughening mechanisms has been provided by Kuntz *et al.* [60], outlining the major forms of toughening in nanocomposite ceramics. Composites containing alumina and zirconia

have been extensively studied in the bulk form, these composites commonly referred to as zirconia-toughened alumina (ZTA) [22].

Microcrack toughening involves the presence of small microcracks that deflect or remove energy from the main crack tip [60]. These microcracks are normally produced by thermal residual stresses in two-phase structures upon cooling. Nanocomposites are particularly effective in toughening a structure as the materials contain many grain boundaries where microcracks are usually generated, thereby maximising the number of microcracks. There is an additional benefit from increased hardness, due to smaller grain sizes according to the well known Hall-Petch equation [65,66], which describes the inverse relationship between grain size and hardness. Nanocomposites may be classified according to the nature of the two phases, it is worth noting that the only fully crystalline alumina-zirconia thin film coating produced thus far has been of the so-called “nano-nano” type where the two phases each form grains interdispersed within each other.

One mechanism particular to zirconia based composites is transformation toughening [22,30]. The transformation from tetragonal to monoclinic and subsequent expansion causes a compressive stress to form within the microstructure. For any crack in the composite structure, the stress fields associated with the crack tip may activate the transformation for any metastable tetragonal zirconia in a microstructure, thus providing a compressive force precisely at the location of the tip. A great deal of work has been focussed on stabilising the tetragonal polymorph within a structure in order to utilise transformation toughening. It has been found that the fracture toughness of alumina can be increased from $4.89 \text{ MPa}\cdot\text{m}^{1/2}$ to $5.88 - 8.12 \text{ MPa}\cdot\text{m}^{1/2}$ through the addition of zirconia [30,67,68]. Extensive studies have been made on the behaviour of alumina-zirconia composites during cutting and subsequent transformations within the zirconia from the tetragonal phase to the monoclinic phase and a stochastic model developed to predict stresses involved in the process [67].

Applications

Alumina-zirconia composites are commonly applied where a ceramic material is required with a combination of hardness and toughness. As thin films, alumina-zirconia has been focused mainly on thermal barrier coatings [69], but have also been

developed for diffusion barriers [3] and high- k dielectric films [5] with suggestions that the same system may also be used for wear resistant coatings [2]. Each application typically requires its own type of microstructure that must be tailored. This thesis is focussed on the development of new nanocomposite thin-film microstructures within the alumina-zirconia system.

Plasmas and Sputtering

“Gas! Gas Captain!
Whatever the Klingon designation for it is,
it is merely ionized gas.”

Captain Spock in *Star Trek VI: The Undiscovered Country*

Plasma Basics

Lieberman and Lichtenberg describe plasmas as “A collection of free charged particles moving in random directions that is, on average, electrically neutral” [70]. There is a wide range of conditions that can induce the formation of plasmas. In the deposition of thin films weakly ionised, low-temperature discharges are of primary interest as distinct from other types, for example high-temperature plasmas, common in nuclear fusion, or low density plasmas, such as the solar wind. In order to achieve the desired plasma, an electric field is applied to a gas, in many cases in combination with a magnetic field. The interactions between the external fields that induce the plasma and the particles within the plasma are complex, as such simplified models are common to characterise the plasma. The starting point for building a model is the macroscopic field equations, *Maxwell's equations*:

$$\nabla \times \bar{E} = -\mu_0 \frac{\partial \bar{H}}{\partial t} \quad \text{Equation 1 [70]}$$

$$\nabla \times \bar{H} = \epsilon_0 \frac{\partial \bar{E}}{\partial t} + \bar{J} \quad \text{Equation 2 [70]}$$

$$\epsilon_0 \nabla \cdot \bar{E} = \rho \quad \text{Equation 3 [70]}$$

$$\mu_0 \nabla \cdot \bar{H} = 0 \quad \text{Equation 4 [70]}$$

Where:

- \bar{E} – Time and space varying electric field vector
- \bar{H} – Time and space varying magnetic field vector
- \bar{J} – Time and space varying current density
- ρ – Time and space varying charge density
- ϵ_0 – Permeability of free space
- μ_0 – Permittivity of free space

Since the plasma is due to an electric field, a charge flow or current must exist. By considering the charge flow across the plasma and assuming that variations in the

magnetic field are negligible then *Poisson's equation* relating the potential to the charge density can be obtained:

$$\nabla^2 \Phi = -\frac{\rho}{\epsilon_0} \quad \text{Equation 5 [70]}$$

Where: Φ – Electric potential
 ρ – Time and space varying charge density
 ϵ_0 – Permeability of free space

Particles in a plasma

Plasma consists of electrons, ions and neutral particles. The particles may be assumed to move independently of each other within the bounds that the plasma must remain macroscopically neutral or quasi-neutral, this is often called the *plasma approximation* [70,71]. Electrons, being light, fast moving species are almost always at thermal equilibrium; ions being heavy, slow moving species are almost never at thermal equilibrium while neutrals may or may not be at equilibrium depending on the plasma [70]. Whether the particles interact with themselves or mainly with the applied electric field depends on the *Debye Length* which is naturally a factor of the density of particles in the plasma and the speed at which the plasma is moving, both of which are important parameters of the plasma itself. It is also worth noting that the speeds at which electrons move are quite high, corresponding to an electron temperature >1000 K, but in low-density plasmas, the particles are so few that little of this heat is transferred to chamber walls. The distribution of particles in the plasma and effect on film deposition has been studied in **Paper 5** where the presence of metal-oxide clusters has been linked to the changes in the stoichiometry of the as-deposited film.

Surfaces immersed in a plasma

Light and fast electrons will accumulate on any surface immersed in the plasma faster than the ions, leading to a negative charge. This charge will repel other electrons and attract ions until equilibrium is reached. This equilibrium negative potential relative to the plasma is called the *floating potential*. All non-earthed surfaces immersed in the plasma will acquire this potential. In a similar way, the plasma will initially loose more electrons to the electrodes than ions, resulting in a positive potential in the plasma. This potential will reduce the flow of electrons to the electrodes which, in-

turn, reduces the positive potential. Eventually a steady-state is reached where the *plasma potential* is the positive potential of the plasma, see Figure 4. The region where the electrons are repelled from the walls, the anode, is known as the *anode sheath*. The plasma sheath parameters such as thickness and potential are related to the plasma parameters at steady state by the *Child Law*, see Equation 6 [70]. Attraction, or acceleration of, positive ions toward a surface leads to ion bombardment and by placing a material of interest at this surface, the deposition process of sputtering is obtained.

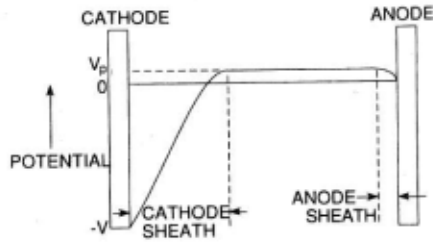


Figure 4: The plasma potential, V_p , and cathode sheath potential [72]

$$J_0 = \frac{4}{9} \epsilon_0 \left(\frac{2e}{M} \right)^{1/2} \frac{V_0^{3/2}}{s^2} \quad \text{Equation 6 [70]}$$

- Where:
- J_0 – Constant ion current across the sheath
 - V_0 – Potential at sheath edge
 - s – Sheath width
 - M – Mass of ions accelerated in sheath
 - e – Charge of an electron
 - ϵ_0 – Permeability of free space

Sputtering

In sputtering, a target of the material to be sputtered forms the cathode, to which a high negative potential is applied [73]. A gas is introduced into the anode-cathode chamber, typically argon but sometimes also krypton, xenon or even a non-noble gas. The potential across the gas causes stray electrons to accelerate toward the anode and collide with the gas atoms along the way, forming a plasma. The collision will result in a positively charged ion and two electrons, if the initial electron has sufficient energy. The resultant electrons will, once again, be attracted toward the anode, while

the resultant ions will be attracted toward the cathode due to the large negative potential. The ions will be attracted through the *cathode sheath*. See Figure 4, and bombard the target surface. The impact of the ions on the cathode causes atoms or ions to be removed, or sputtered, from the target in addition to secondary electrons, see Figure 5.

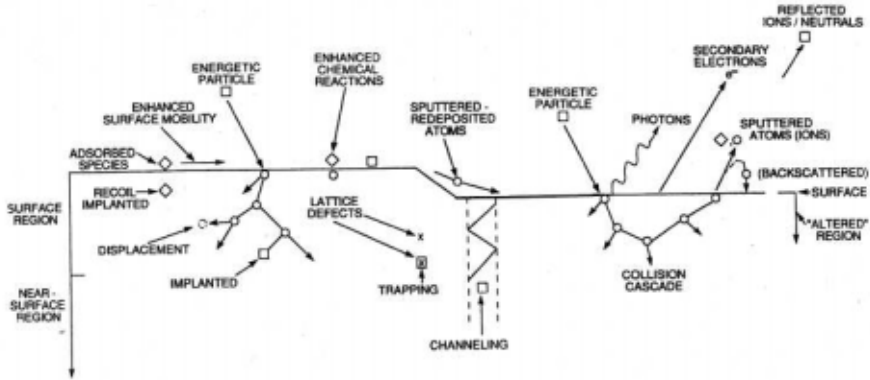


Figure 5: Particle interactions in sputtering [72,74]

The entire process results in the formation of several more charge carriers that continue the process in the gas leading to a self-propagating ionised gas, or plasma. The remaining particles that are expelled from the target as a vapour travel to the material being coated, the substrate, and condense to form the coating.

Sputtering belongs to a class of techniques known as physical vapour deposition (PVD) since the primary mode of film synthesis is physical as opposed to chemical methods [72]. A schematic of a typical deposition system is shown in Figure 6. The system shown was used to produce the films in **Paper 2** and perform the study of plasma deposition flux in **Paper 5**.

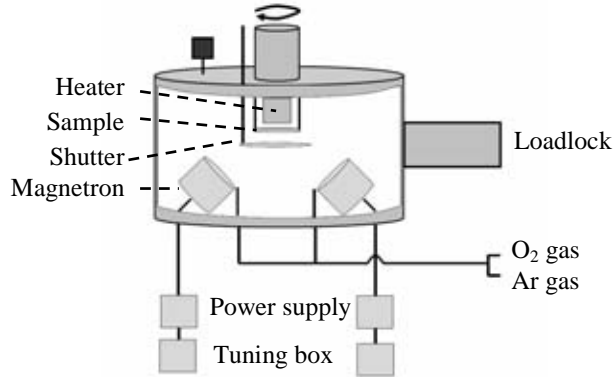


Figure 6: Typical sputtering deposition system
(Equipped with radio-frequency power supplies, see later section)

This is, of course, a simplified model of sputtering, there are many factors which can affect plasma characteristics, including the ability to self-propagate, these include gas pressure, electrode separation, mean free path of particles in gas, breakdown voltage of the gas and cathode characteristics [75].

Magnetron sputtering

If a magnetic field is applied to the sputtering plasma then the electrons normally travelling in a direct path describe a helical path instead*. If magnets are placed behind the sputter cathode then the electron is subject to a radially decreasing magnetic field in combination with the applied electric potential, or field, see Figure 7.

* Since the magnetic force acts perpendicular to the direction of the electric current as governed by the *Lorentz Law*.

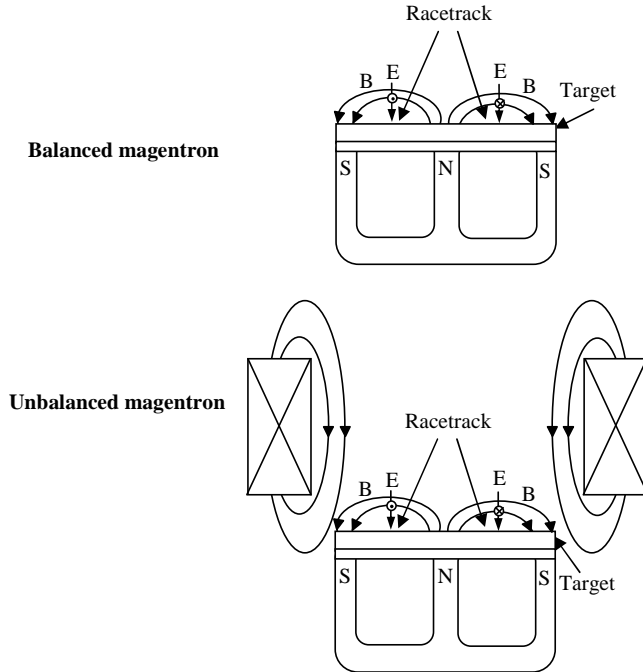


Figure 7: Magnetron sputtering cathode configuration [75]

The combination with a magnetic field and electric field linearly decreasing from the surface results in the electrons describing a half-helix originating and returning to the cathode surface [75], see Figure 8. The electrons are hence confined close to the target surface, thereby increasing the degree of ionisation as well as the sputtering rate and thus increasing the deposition rate. This configuration is commonly referred to as magnetron sputtering, as opposed to conventional, or diode, sputtering. Magnetron sputtering typically operates at lower voltages, 500 – 600 V, compared to several kV in conventional diode sputtering [76]. The increase in sputter rate may be an order of magnitude greater than that of conventional sputtering and lower pressure regimes can be used [72,73]. A secondary effect is that the electron bombardment of the substrate and the chamber walls is minimised. It should be noted, that the confinement of electrons in a magnetron leads to a circular track, known as a racetrack, on the surface of the target that may not be of the same composition as the remainder of the target [77].

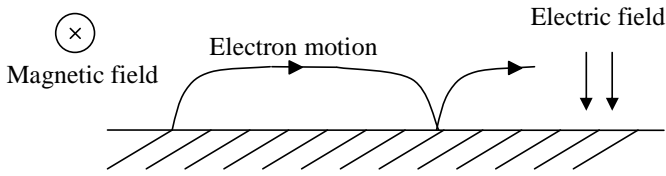


Figure 8: Motion of electrons in a planar magnetron [73][†]

Reactive Sputtering

The addition of a chemically reactive gas, such as oxygen or nitrogen, into the deposition chamber can be used as a method for depositing compounds such as alumina without the need for a compound target [72], this variant is known as reactive sputtering. Synthesis of compounds with reactive sputtering is generally preferred since the overwhelming majority of compounds can not be produced in the form of a sputtering target. Noting also that in the models presented thus far, the target is the cathode and thus, must be a conductor, and the vast majority of compounds are *not* conductors, hence reactive sputtering is the preferred method for depositing compounds. This process is, however, significantly more complex than sputtering a metal or compound target with a noble gas.

A number of changes in the plasma occur when a reactive gas is allowed into a chamber. These changes can be related to the reaction of the gas with either target or substrate, noting that they do not occur within the plasma as there are no mechanisms that dissipate the heat of the reactions and simultaneously conserve momentum and energy [77]. Changes in the reactions with the target are the most critical when comparing reactive sputtering to metallic sputtering as the compounds formed inevitably produce fewer sputtered atoms for each incident ion, that is, the compounds have lower *sputter yield*. When sputtering compounds, the majority of energy goes into breaking bonds and accelerating the resultant secondary electrons, hence a higher *secondary electron yield* results, but in doing so, less energy is available for sputtering atoms and hence the deposition rate is significantly lowered. The amount of compound formation on a metallic target becomes an important parameter, this is

[†] Sputtering systems in this thesis were circular. The change in geometry does not affect the physics, other than adding the radial dimension as a parameter.

investigated in **Paper 4**, where compound formation on the target forms part of a mass-balance model for sputtering.

Target poisoning and hysteresis

Initially, a metallic target will not have any compound on the surface but upon reactive sputtering, compound formation will begin. Provided the rate of compound formation is slower than the rate of compound sputtering, then the target will continue to behave as a metallic target, noting that the film formed is then mostly metallic with some compound formation on the surface. In order to produce a stoichiometric compound, the reactive gas flow rate must be increased. In doing so, more compound will form on the target surface. This will cause a decrease in the sputtered atoms and the amount of reactive gas consumed. At some point, the target will be completely covered by compound and the gas consumed will drop sharply coupled with a marked reduction in the sputter rate. The target is referred to as being *poisoned* at this point and will remain so even when the reactive gas flow is decreased until there is insufficient flow to react fully with the target. This occurs at a different flow to where the layer formed, hence a hysteresis results, see Figure 9. It should be noted that for a magnetron sputtering system the flow to the target is not uniform and hence certain parts of the target may be poisoned while others may not be poisoned [77 – 79].

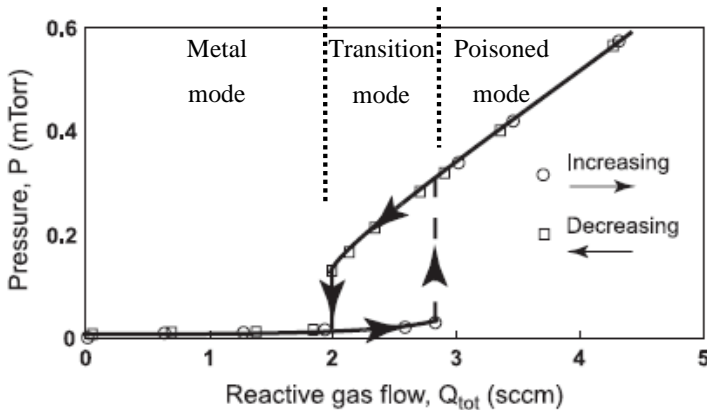
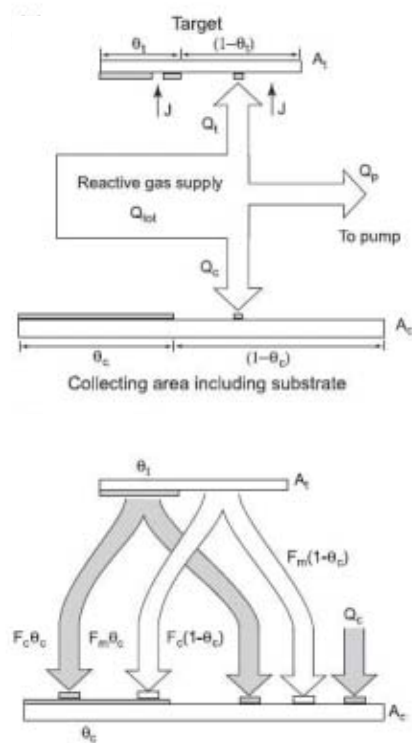


Figure 9: Hysteresis in reactive sputtering due to target poisoning [80]

Berg model for reactive sputtering

Modelling of the hysteresis in reactive sputtering has been achieved through what is known as the Berg model for reactive sputtering [80 – 82]. The model considers the fractional coverage of both sputter target and substrate with compound. The incoming gas flows to the target, substrate and the gas flowing through the system to the pump are also considered. A mass flow balance is then taken in order to determine the parameters of a sputtering process. This simple and, in certain aspects, crude model[‡], see Figure 10, has proved to accurately describe experimental results regarding the hysteresis in a reactive sputtering process. Indeed, from the model, the effect of changing target material, reactive gas, pumping speed, substrate distance, target ion current and target area can be determined. The model has since been expanded to include reactive co-sputtering from two targets or alloy targets and sputtering a single target in two gases to form multiple compounds. In **Paper 4**, this model has been expanded to consider the sputtering of two targets in a dual-gas environment. Here, the addition of nitrogen into the sputter process was found to suppress the hysteresis effect in the aluminium-zirconium oxide deposition process. The nitrogen incorporation into resultant films was minimal, albeit non-zero. Such development in the process may be useful in the long-term future to reduce target poisoning in industrial systems, without partial-pressure control or over-pumping (see next two sections) [83].

[‡] Many assumptions are made to the model in order to ease the burden of calculation. Such assumptions include, although are not limited to, a single compound monolayer target coverage, uniform gas kinetics with simple chemical reactions, two-atom molecular sputtering for compounds and uniform secondary electron emission coefficients.



- A_c – Receiving area
- A_t – Target area
- θ_t – Fraction of target with compound molecules
- θ_c – Fraction of receiving area with compound molecules
- J – Ion current density
- Q_{tot} – Total supply rate of reactive gas
- Q_t – Reactive gas consumption of target
- Q_c – Reactive gas consumption of collecting area
- Q_p – Reactive gas consumption of pump
- F_m – Sputtered elemental species per unit time
- F_c – Sputtered compound molecules per unit time

Figure 10: The Berg model for reactive sputtering, (above) important parameters in the model (below) typical notations for flux calculations [80]

Partial-pressure control

A method of avoiding target poisoning involves the measurement of one of the process parameters, such as the reactive gas partial pressure, and use of a feedback signal loop to constantly correct the flow of reactive gas into the system. In doing so, the deposition can be maintained in the transition region, ideally close to the turning point where a metallic target actually enters into the transition mode, so as to achieve high deposition rate while maintaining the stoichiometry of the compound being deposited [10]. In this thesis, specifically **Paper 3**, the oxygen partial-pressure was measured with a lambda probe [84,85]. This signal was then coupled to a proportional-integral-derivative (PID) controller in combination with a piezoelectric actuator to the oxygen flow valve, see Figure 11. With this apparatus, any detected increase in the oxygen partial-pressure, indicating less target sputtering, causes the flow valve to close, returning the deposition to the original point. While this method was successful in producing near-stoichiometric compound films, there are at least two shortcomings affecting the applicability in an industrial context. Firstly, as the target becomes slowly covered by compound, the oxygen flow is decreased, but not to the extent to return to metallic mode sputtering, so the target eventually becomes poisoned if the process is run for a sufficiently long time. Secondly, there is a certain delay in the measurement of oxygen partial-pressure and the reaction of the valve, this is necessary to ensure that flow is not changed in response to momentary changes or inhomogeneity in oxygen partial-pressure and in this time either a metallic film may result or further target poisoning.

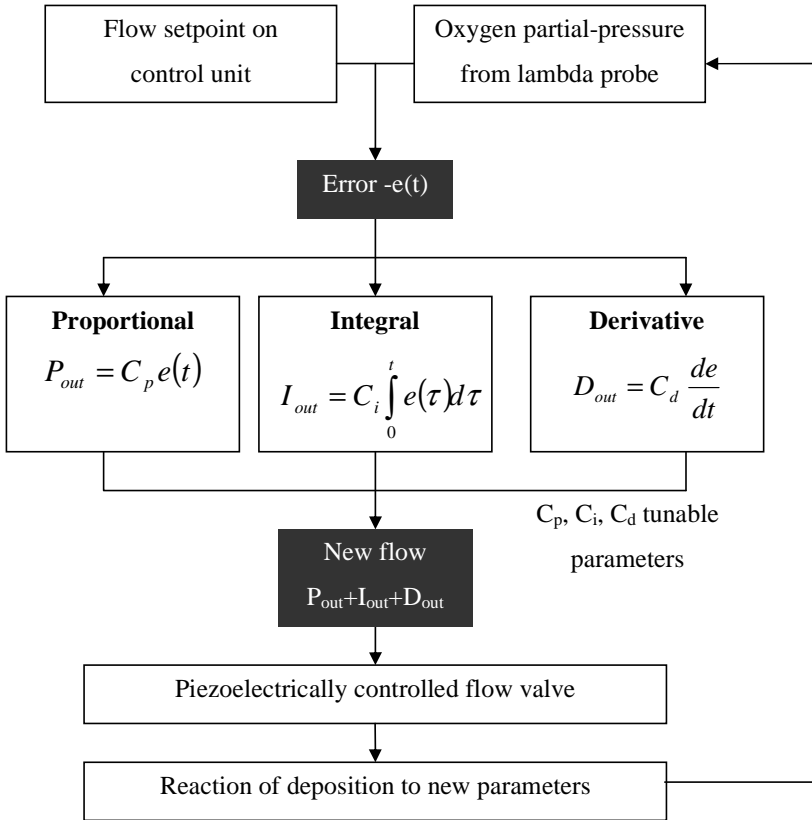


Figure 11: Process for PID control used in **Paper 3**

Over-pumped systems

If the pumping speed of a deposition is set such that the rate at which the reactive gas is pumped away dominates over compound film growth rate on the target, then the hysteresis region will progressively be elongated to a point where the pumping speed is sufficiently high that the reactive gas does not adequately form a compound layer on the target. Hence, the hysteresis disappears. This effect is evident in the vacuum chambers used for **Papers 1, 2 and 5**, see Figure 12. Since no hysteresis was evident in the sputtering process, over-pumping may have also affected the results in **Paper 5**. While such a solution is convenient for avoiding the problems associated with poisoning on a laboratory scale, it is hardly applicable to industrial deposition systems which are typically much larger.

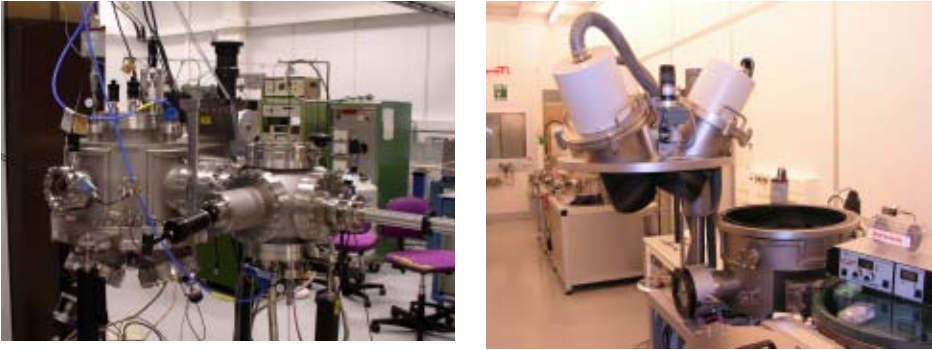


Figure 12: Laboratory-scale vacuum chamber used in **Papers 2 and 5** (left) and industrial pilot-plant vacuum chamber used in **Papers 3 and 4** (right)

Capacitive Plasmas – Radio-Frequency

In the model presented so far, a constant electric field has been assumed: the cathode and the anode remain fixed and a direct-current (DC) power supply is used to create the electric potential. Since the system is an electric circuit then all components of the system must be electrical conductors [72]. This means that insulators, such as alumina or zirconia cannot be cathode materials, since charge will simply build up on the insulating surface and lead to unstable arcing. A solution to this problem is by oscillating the electrical field with a certain frequency. In doing so, charge build-up is avoided and insulators may be sputtering [72]. Here, the important parameter becomes the *capacitance*, rather than the conductivity, and hence, insulators may be sputtered. Many different frequency regimes can be used to oscillate the electric field, radio-frequency (RF) lies between the megahertz and gigahertz range and has been used in **Papers 1 and 2** to deposit films.

The already complex plasma becomes even more so when the electric field has a time-dependent frequency. Light electrons move with the oscillating field but heavy ions are not able to follow the field and only respond to time-averaged potentials [70]. The electrons have enough energy to ionise the sputtering gas, reducing the need for secondary electrons to sustain the plasma, allowing lower operating pressures compared to DC sputtering [73]. Another effect of RF sputtering is the *self-biasing* of the target to a negative potential [72]. In the positive half of the cycle, the electrons are drawn toward the target, causing collisions, while in the negative half of the cycle,

the remaining ions are not affected to the same extent. The result is a negative potential.

The RF sheath

Since the potential is oscillating with a certain frequency, it is only natural that the sheaths in an RF plasma also oscillate with a time dependent frequency [86]. In addition to this, a bimodal distribution results in the ion energy distribution [87]. The dynamics of the sheath are hence, significantly different from the sheaths in DC sputtering. The sheath parameters are typically calculated by integrating Poisson's equation and adding boundary condition that the electric field is zero at the sheath edge. Assuming that the voltage drop across the plasma is small relative to the voltage drop across the sheaths, the combined voltage across both sheaths, and hence, the voltage across the discharge can be expressed by:

$$V_{ab} = \frac{2en\bar{s}s_0}{\epsilon_0} \sin(\omega t) \quad \text{Equation 7 [70]}$$

- Where:
- V_{ab} – Voltage drop across both sheaths
 - e – Electron charge
 - n – Plasma density
 - \bar{s} – Average (DC) sheath width
 - s_0 – Constant
 - ω – Cyclotron frequency
 - t – Time
 - ϵ_0 – Permeability of free space

Since ions flow according to the time-averaged potential such as the RF potential, ions will steadily flow through both the cathode and anode sheaths. As there is no charge build-up, and there are no electrons in the sheath, then electrons must reach the electrode at some point to neutralise this charge. This implies that the sheath, while continuously varying, *collapses to near zero* at some point during the RF cycle [70], see Figure 13.

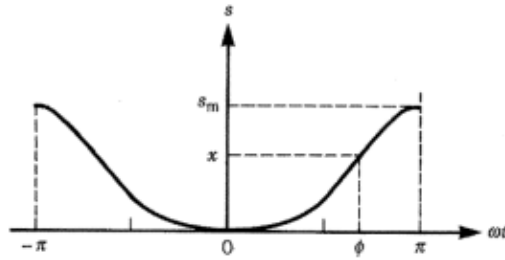


Figure 13: Sheath thickness dependence with time [70]

DC bias

The anode area, typically the chamber walls of the deposition system, is significantly larger than the cathode area, typically the sputtering target. To a rough approximation[§], the anode sheath capacitance is larger than the cathode sheath capacitance. This means that the voltage, inversely proportional to the capacitance, differs between the anode and the cathode sheath. As such, a DC bias voltage with respect to ground is attained at the electrode that is driven by the power supply. This is often known as simply the DC bias and is readily measurable. The DC bias is often used in RF reactive sputtering in two contexts:

- The DC bias is greatest when the entire circuit is correctly tuned
- DC bias changes markedly whether a target is an insulator or conductor and can be an indication of target poisoning

Matching networks

While RF sputtering does solve numerous problems associated with DC sputtering, there exist many problems in applying a RF power source to a target. RF circuits are much more complex than DC circuits, see Figure 14, with an equivalent expression for the power transferred shown in Equation 8. It is obvious from this equation that the maximum power transfer occurs when the discharge reactance is zero and the discharge resistance is greater than the source resistance. Now, typically the discharge reactance is *not* zero and the discharge resistance is much smaller than the source resistance [70]. Hence a matching network consisting of a shunt capacitor and

[§] The sheath thickness is also dependent on voltage which is in turn a function of capacitance. A more rigorous calculation will lead to a *Child Law* dependence on the thickness of the capacitive sheath [70].

series inductor is normally inserted into the system to match the parameters and to ensure efficient power transfer and this network can be tuned to the individual plasma parameters.

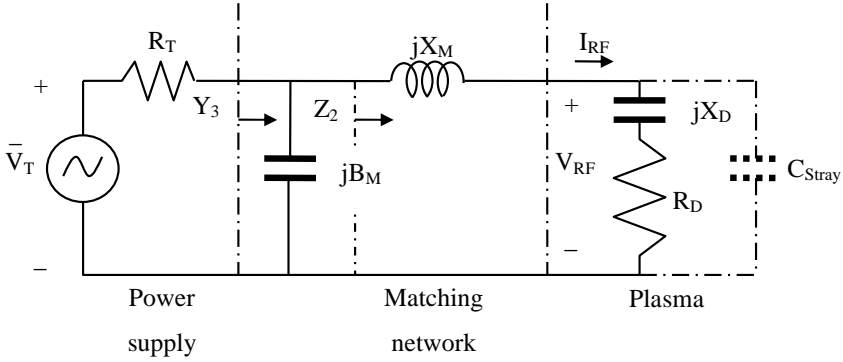


Figure 14: Typical matching network for RF discharge [70]

$$\bar{P} = \frac{1}{2} |\bar{V}_T|^2 \frac{R_D}{(R_T + R_D)^2 + X_D^2} \quad \text{Equation 8 [70]}$$

- Where:
- \bar{P} – Power transferred
 - \bar{V}_T – Complex voltage amplitude of power source
 - R_D – Discharge resistance
 - R_T – Source resistance
 - X_D – Discharge reactance

Characterising Plasmas

Langmuir probe

Electrostatic probes such as the Langmuir probe are quite common in the measurement of plasma parameters [88,89]. A probe consists of one or more electrodes that are inserted into the plasma. A voltage potential is applied to the each electrode, this causes the formation of a sheath around the electrode. By measuring the current response to the potential and taking the radius of the collector, or sheath, the distribution of velocities of the ions arriving at the sheath boundary and total potential drop of the sheath can be calculated. From here the speed at which electrons move, known as the *electron temperature*, and the *plasma density* can be calculated. So as not to disturb the plasma during measurement, the probe tends to be constructed of a thin wire with radius smaller than the Debye length. Taking several electrodes at

the same time allows the mapping of the spatial distribution of plasma properties. For Langmuir probe measurements of RF plasmas, a small matching network is applied to the actual probe to ensure that the probe oscillates with the same frequency as the plasma, hence forming an electrostatic probe [90].

Optical emission spectroscopy

Since the plasma consists of a range of excited particles, including ions, electrons and neutrals, that combine and collide, a range of photons are constantly being emitted from the plasma. The energy emitted will depend on the particular excited particle. By cataloguing the emission from a plasma and coupling this to a model for the excitation and relaxation processes in the plasma, a clear image of the plasma can be obtained [89,91]. In this “image”, the particles present, the energy states and energy distribution are included.

Mass spectrometry

An alternative, or more precisely a complement, to both the previous methods for characterising a plasma involves the collection of individual particles from the plasma, such a technique is known as mass spectrometry, see Figure 15 [92,93]. An electrical probe, generally consisting of a cylinder with a small orifice is inserted into the plasma. Particles from the plasma will enter into this orifice as a matter of course through their normal motion within the plasma, noting that since the probe is a surface a sheath will also form on the probe surfaces. If neutrals are being analysed, an ion source is present to convert the neutrals to ions. The ions, or ionised neutrals, pass through an electrostatic energy filter or a quadrupole mass filter to separate certain energy or ions of a particular mass:charge ratio. The remaining current is then scanned, typically the energy distribution of a particular particle mass, or the number of particles with a particular energy are displayed. The former was used extensively in **Paper 5** in order to analyse the plasma and to further understand differences in the phases formed in **Papers 1 and 2**. Typically, and in this case, a mass spectrometer is differentially pumped in order to increase the mean-free path of the particles, boosting the intensity, as the particles would otherwise collide with other particles causing a decrease in intensity. Noting that in the case of **Paper 5**, the off-axis geometry of the magnetrons posed special problems to the detection of particles. Since the flow of particles in a sputtering system is directed away from the magnetrons, the majority of

the flow is directed toward the walls of the cylinder in the mass spectrometer, rather than directly into the filters. The result is decreased intensity and the loss of high-energy particles, which proceed directly into the wall of the mass spectrometer without being diverted by the filters.

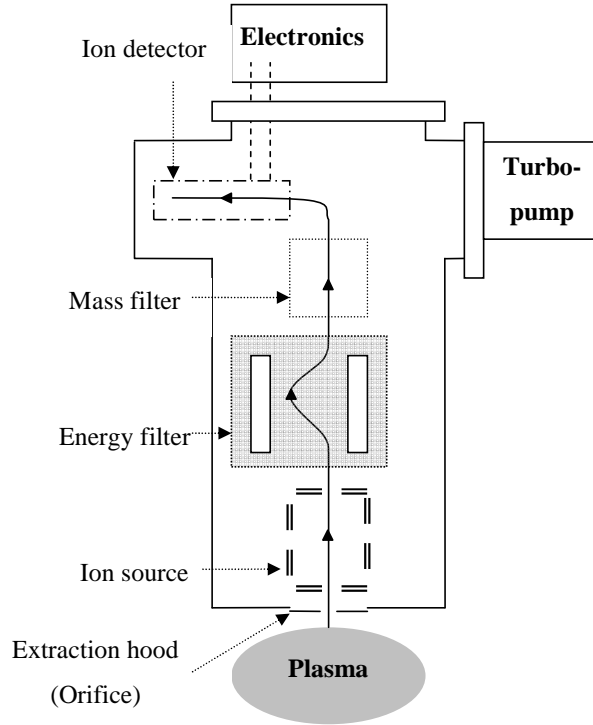


Figure 15: Schematic of a mass spectrometer [94,95]

Thin Film Growth

“Men can do all things if they will”
Leon Battista Alberti

Novel Structures

Once a desired material is sputtered, the particles that pass through the plasma will eventually reach the material to be coated, the substrate. The energy that the particles have upon reaching the substrate is measured at the substrate position, see previous chapter and **Paper 5**. Three basic growth models exist, the *Volmer-Weber* mode, where the film grows as small islands, the *Frank-Van der Merwe* mode, where the film grows layer-by-layer and *Stranski-Krastanov* mode, a mixture of the two former modes [72]. The Volmer-Weber mode is most relevant for this study, and proceeds as follows [75]:

1. *Adsorption* of particles and clusters onto the surface, kinetic energy of particle used in adsorption process;
2. Movement of species on the surface as the arriving species are not in equilibrium with growth surface. Species interaction amongst themselves resulting in larger clusters;
3. Clusters either desorb due to thermodynamic instability or grow with the aid of collisions with other arriving species. Past a critical size, the cluster remains as it is large enough to be thermodynamically stable. This is known as nucleation;
4. Stable nuclei grow in number and volume on the surface. Nuclei begin to form islands;
5. Small islands coalesce, with or without faceting, to minimise surface area and hence surface energy. New nuclei may form on the surface of this new area;
6. Larger islands grow bridges, leaving channels and holes uncovered, these becomes pores if not filled by mobile species.

The key in the above process is the mobility of the arriving species on the surface. This is controlled by either varying the energy of the arriving species, or the energy supplied by the surface [96]. The easiest way to achieve this is to change the temperature of the substrate; a warmer substrate imparts more energy to the arriving species than a colder substrate. To design novel nanocomposite structures, as per the

aims of this study, the mobility of species on the surface must, however, be restricted so that thermodynamically stable structures do not form hence the substrate temperatures are often restricted to relatively low values, $<500\text{ }^{\circ}\text{C}$.

Structure zone models

Empirical structure zone models have been developed to describe the microstructures formed with respect to energy of arriving species, expressed as the sputtering gas pressure, and the mobility of species of the surface, as reflected in the substrate temperature [97 – 99]. An example is shown in Figure 16. The columnar structure typical of competitive growth, shown as “zone T” in Figure 16, is evident in all the crystalline films produced in **Papers 1 – 3** and will be discussed further.

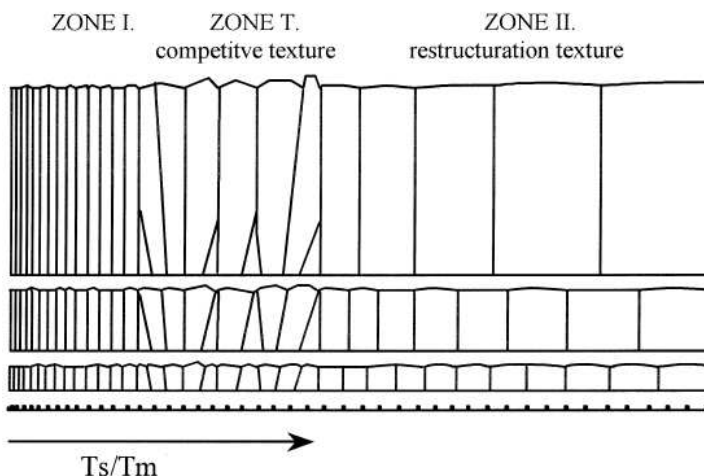


Figure 16: Structure zone model developed by Barna and Adamik [99] for pure elemental films relating substrate temperature (T_s) and material melting point (T_m)

In the competitive growth mode, larger islands coalesce in order to minimise the energy per atom by reducing the surface area and interface energy [100]. This is achieved through surface atom diffusion and grain boundary motion. Initially, as the grain boundaries come into contact, they become immobile, this causes unfavourable growth orientations to stop growing. The orientation and size of individual crystallites will determine their behaviour during the growth process. Adatoms on the surface of a crystallite diffuse easily on low surface-energy planes, and have little probability of sticking on such planes, rather diffuse to other planes or grain

boundaries. Low-diffusivity surfaces are generally those that have more lower-potential-energy sites and high surface-energy. These surfaces have a higher probability of retaining atoms and hence, grow faster. Along grain boundaries, the diffusion is more limited, as the structure is less open and atoms do not tend to move from this boundary. A pronounced columnar structure with grains elongated on the low-diffusivity surfaces result. Note that the column width can be a measure of the energy available for surface diffusion in a self-organising growth mode. In multi-component systems, particularly in alumina-zirconia, where the materials are generally not compatible, the presence of the other phase tends to interrupt the growth along low-energy planes by virtue of surface segregation and cause renucleation, hence smaller grain size [100].

Structural Morphology

The formation of columns is often associated with two other morphological features found in the films deposited in this thesis, facets and pores. Both are the result of a combination of the restricted mobility and the geometry of the sputter deposition system used, see Figure 17. The restricted mobility means that atoms cannot diffuse from the exposed areas to the shadowed areas, and hence, the areas remain unfilled. Columnar growth is often perpendicular to the substrate when there is sufficient mobility [72]. In **Paper 3**, the mobility was presumably lower than in **Papers 1 and 2** due to the lower substrate temperature, ~ 300 °C compared to 450 °C, and the lower ion energy associated with DC sputtering compared to RF sputtering, a few electron volts compared to 10 – 15 eV. This change in mobility may partially explain the formation of different metastable phases when RF sputtering is substituted with DC.

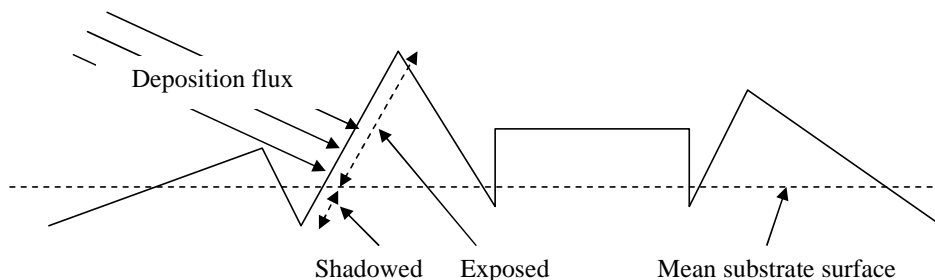


Figure 17: Formation of facets and pores [101]

Crystallographic Effects

Preferred orientation

If the barrier to nucleation is low, then randomly oriented islands may arise [100]. The grain orientations depend on a range of factors including the nature of the substrate, particle energy arriving at the surface and geometry of actual deposition system [72]. In **Papers 1 and 3**, preferred crystallographic orientation is observed in the cubic and monoclinic zirconia phases respectively. The reasons behind the preferred orientations are generally related to the low mobility that restricts movement of adatoms on the growth surface.

Metastable phases

The formation of metastable phases in the alumina-zirconia system due to the lattice restraint is known in bulk materials [29]. In addition to this restraint, there is the crystallite size effect previously mentioned [31]. In **Paper 1**, the cubic zirconia phase was observed after the addition of alumina into the film. Here, it was suggested that the alumina separated from the zirconia matrix, restraining the zirconia matrix from forming the thermodynamically stable monoclinic phase. This was further developed in **Paper 3** which linked the mobility of aluminium in the zirconia matrix to the formation of the tetragonal zirconia phase.

In addition to the size restraint, there were indications for an oxygen deficiency in the films deposited from ceramic targets in **Paper 1**. The reasons behind this deficiency were investigated in **Paper 5**, being linked to the presence of metal-oxide clusters in the plasma and subsequent availability of oxygen on the substrate surface. This oxygen deficiency contributed to the prevention of the formation of the thermodynamically stable monoclinic zirconia phase.

Amorphous films

When the mobility of the atoms is reduced further, such as in the case of depositions at low substrate temperature, or in cases where alumina and zirconia were mixed in almost equal proportions, then amorphous films resulted. The diffusion distance of atoms is simply too great for enough atoms to coalesce and form a crystalline phase with long-range order. While amorphous films can be of interest for a number of applications, such as metallic glasses [102] or semiconductors [103], the aim of this

work was the synthesis of novel structures and hence amorphous films were not of immediate interest. In **Papers 1 and 2**, the amorphous structure could be avoided by increasing the diffusion range of the adsorbed species through increasing substrate temperature. A limit was, however, often reached, since higher temperatures also promote inter-diffusion of the substrate and film elements, which was undesirable.

Analysis Techniques

“To see is not a question of the senses”
 John Coetzee: *The Master from St Petersburg*

X-Ray Diffraction

This technique is commonly applied for the analysis of the structural properties of materials. The technique is popular as it is both non-destructive and can be applied to almost any solid sample without any special preparation techniques. The information provided by x-ray diffraction (XRD) is primarily concerned with *periodicity* in a structure. Each atom in a periodic structure acts as a point of scattering for waves. These scattered waves may interfere constructively to form sharp peaks in intensity. The requirements for constructive interference are described by *Bragg’s law*, as given below in Equation 9 with a simplified model given in Figure 18. XRD provides primarily information regarding crystal structure, since periodicity and symmetry are major components of ordered crystal structures. Distortions or alterations to the periodic structure can also be observed through distortions in the x-ray diffractogram, this provides information regarding grain size, epitaxy and texture and even residual stress [104,105].

$$n\lambda = 2d \sin \theta \qquad \text{Equation 9}$$

- Where:
- n – Integer
 - λ – Wavelength (for x-rays from a Cu K α Source 1,54Å)
 - d – Distance between the periodic atoms
 - θ – Diffraction angle

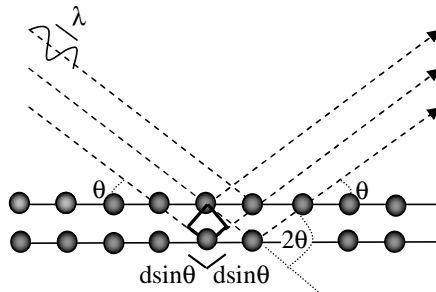


Figure 18: Diffraction in an atomic lattice as described by Bragg’s law

Alternatively, XRD can be viewed through the von Laue construction and the Ewald sphere. In reciprocal space, a sphere is drawn with origin at the tip of the incident x-ray vector, \mathbf{k} . X-ray peaks are located at points where the edge of the sphere crosses the reciprocal lattice, see Figure 19 [106]. The von Laue / Ewald sphere method and Bragg method of viewing x-ray diffraction are essentially equivalent.

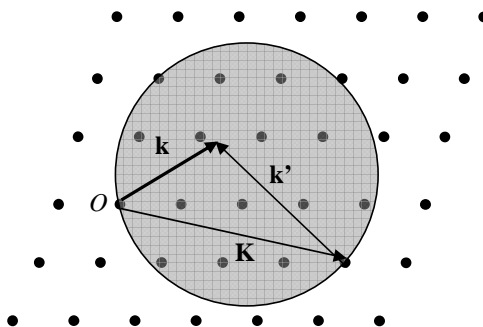


Figure 19: von Laue / Ewald sphere representation of diffraction [106]

\mathbf{K} is diffraction vector, \mathbf{k} is the incident x-ray vector

Bragg's law is not restricted to XRD. It is indeed simply a mathematical description of the requirements for constructive interference from an array of atoms. All waves with wavelength approximately equivalent to the distance between atoms (or less) will feature such peaks in intensity characteristic of Bragg reflections. An additional consideration should also be made to destructive interference from such an array of atoms. Another mathematical description, the *structure factor*, is often used to determine where peaks that fulfil Bragg's law do *not* appear due to such destructive interference. Consideration should also be made to the spatial resolution of XRD, which is limited by the interaction volume of incident x-rays. In practical terms, structures of less than ~5 nm cannot be observed with XRD. This has been observed in **Papers 1 – 3**, where crystalline films did not readily show distinct peaks under XRD due to the limited size of the crystallites.

There are many methods of rotating a sample while performing XRD analysis shown below in Figure 20. Each method provides different information regarding the crystal of interest. The following are the most common geometries:

- θ - 2θ the axis
- ϕ rotation of the sample
- ψ tilting of the sample

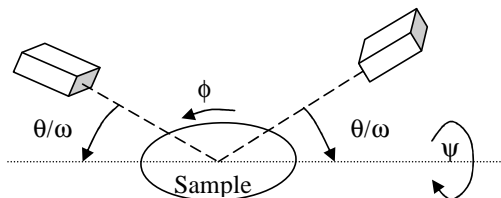


Figure 20: Possible rotation angles for x-ray diffraction

θ - 2θ

The most common type of XRD performed is a so-called θ - 2θ scan. In this method, both ϕ and ψ are fixed at particular values. The incoming beam angle, ω ($=\theta$), and the reflected angle that is scanned, 2θ , are varied in tandem. In practice, the x-ray source is fixed; the sample moves along the θ axis while the detector also moves on the same axis at twice the speed. In vector space, one can visualise the incident wave vector, \mathbf{k} , remaining constant, while the reciprocal lattice is rotated (as the crystal rotates around θ). As the Ewald sphere cuts a reciprocal lattice point, a peak is formed [106]. This technique has been used extensively to catalogue the phase composition of the films produced in **Papers 1 – 3**. In addition, a change in the x-ray optics allowed differentiation between the cubic and tetragonal zirconia phases. This has been achieved through making measurements of the full-width at half-maximum (FWHM) for various peaks. In the tetragonal phase, the 002 and 110 peaks have similar, but different lattice plane spacing. It is common in thin films that the peak spreading due to small grain size is large and hence these two peaks may be observed as a single peak. The FWHM of this peak should, however, be larger than the 101 peak if the two peaks have combined into a single peak. If this is not the case, as in **Paper 2**, it can be concluded that the cubic zirconia phase is present.

Grazing-incidence

The interaction depth of x-rays beams incident onto a material can be minimised to a depth $< 1000 \text{ \AA}$ by using a different geometry known as grazing-incidence x-ray diffraction (GIXRD) [107]. This geometry alleviates problems typical to θ - 2θ scans

in thin film samples of substrate peaks dominating all other peaks as the interaction depth is restricted exclusively to the film. The incoming beam angle, ω ($\neq \theta$), is fixed in this geometry at a low angle, usually $1 - 4^\circ$ [108].

While GIXRD minimises substrate effects, the intensity is also reduced which means that scans are typically much longer than normal θ - 2θ scans. Additional complications are also raised during analysis of textured films; the diffraction vector, \mathbf{K} , is no longer perpendicular to the surface for all 2θ values as in a normal θ - 2θ scan, see Figure 21. As a corollary, the peak information comes from different grains for different 2θ values. Consequently, analysis of preferred orientation is significantly more complex since peak heights may not correspond to reference values. Indeed, in the case of **Paper 1**, the 200 peak in cubic zirconia was not present due to the special GIXRD geometry and preferred orientation in the films. GIXRD was used extensively in **Papers 1 – 3** as a complement to θ - 2θ scans.

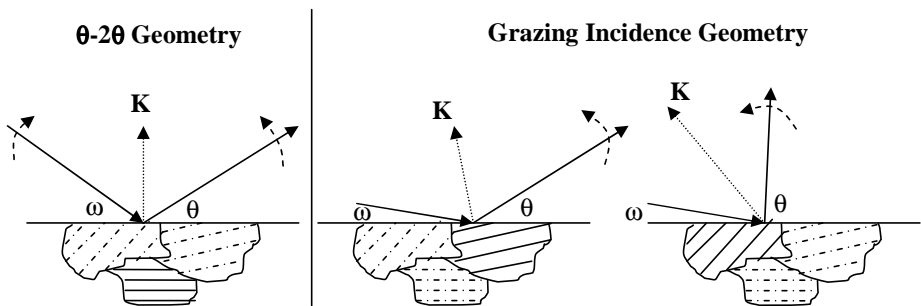


Figure 21: Geometry of the GIXRD showing variation of diffraction vector, \mathbf{K}

Pole figures

A pole figure provides information regarding preferred orientation or epitaxy in a film. A pole figure can be measured for each crystalline peak that is present in the material. The incoming beam angle and reflected beam angle, θ and 2θ , are fixed at a particular value corresponding to an expected peak. Rotation around ϕ is performed for each ψ value. In doing so, the orientation of the planes corresponding to that peak is determined. In a polycrystalline material, a pole figure would show merely diffuse intensity as planes of the same type in different grains are oriented in a random fashion with respect to each other. When a material, or film, has some preferred

orientation or epitaxy, then distinct peaks will emerge in the pole figure. The result can be displayed in 2, 2.5 or 3 dimensional plots. An example is shown in **Paper 1**, where a pole figure is shown for the 200 peak in cubic zirconia.

ψ - 2θ

An alternative to pole figures for the analysis of films with preferential orientation is a ψ - 2θ map [109]. Instead of scanning only ϕ and ψ for only one peak, a θ - 2θ scan is performed for a range of ψ values. In doing so, several peaks with similar plane spacing can be scanned at the same time resulting in several distinct peaks. The angular relationships between such planes with similar plane spacing can be elucidated and related to the theoretical angles between the planes in a structure to confirm a proposed structure. This technique is demonstrated in **Paper 3** when identifying the monoclinic zirconia phase. A pole figure of singular peaks resulted in a single diffuse ring, while the ψ - 2θ map highlighted the differences between the 002 and 020 peaks in monoclinic zirconia, which have similar spacing.

Transmission Electron Microscopy

The transmission electron microscope (TEM) is a powerful technique for investigating materials on the nano scale. The key benefit in using an electron source is that the wavelength is significantly smaller than other wave forms such as x-rays or visible light [110]. Direct imaging of the lattice of a particular material is thus possible. The TEM is the electron analogue of the desktop optical microscope in many ways and a simplified TEM arrangement is shown in Figure 22.

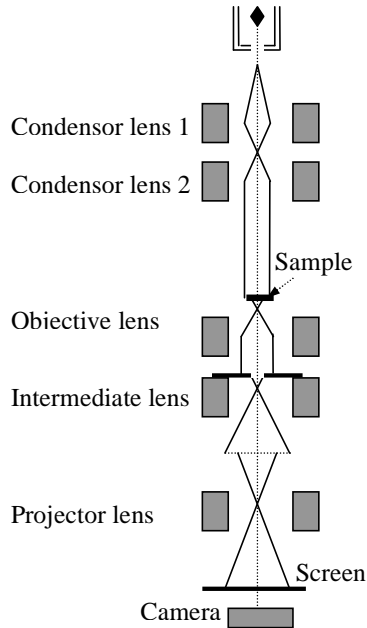


Figure 22: Simplified transmission electron microscope layout [111]

Sample requirements

A key requirement for TEM samples is, naturally, electron transparency, as a thick sample would cause too many interactions leaving no intensity in the transmitted beam. Thin samples also minimise the risk that two different features, say two different grains, overlap in the path of the electron beam, thus reducing confusion in the projected image [112]. A thick sample also increases the risk that an electron is scattered on multiple occasions, which confuses the image. Samples are generally prepared by a combination of mechanical abrasion and ion etching. Damage to the sample is always a consequence of such thinning techniques due to the mechanical forces and thermal energy that is required to remove material, in addition to implantation effects due to the ion etching [110]. The key aims in each preparation step are thus two-fold: to remove the damaged layer from the previous step, and to provide a progressively finer, that is, flatter, surface. The risk does, however, remain that the sample can be considerably altered by the sample preparation techniques.

Care must also be taken to ensure that the prepared specimen is representative for the material being studied since the ultra-thin specimens analysed with TEM may be

relieved of stresses present in a sample, given that elastic restraint is relieved when surrounding material is removed. The zirconia phase selection is sensitive to the elastic restraint [31] and when the surrounding material is removed during sample preparation, there exists a risk that a phase transformation may occur. In the work in **Papers 1 – 3**, care was taken to ensure that any metastable zirconia phases did not transform to the stable monoclinic phase during sample preparation, results from the TEM were compared with those obtained through XRD, prior to TEM sample preparation. Another example is shown in **Paper 1**, where crystallisation of amorphous film material occurred due to the energy of bombarding ions during final thinning. Chemical analysis performed in the TEM may also be distorted since atoms in the sample may be preferentially sputtered or mixed across interfaces by the ion bombardment.

Diffraction imaging

When the electron beam is incident on the sample, all illuminated parts of the sample will act as scattering sources. Interference causes coherently scattered beams when Bragg's law is fulfilled. The coherently scattered beams are recorded as a "spot" pattern residing in the back focal plane. This is, again, analogous to the optical microscope and apertures can be placed in the back focal plane to select either the central, transmitted or non-scattered, spot (*bright-field diffraction imaging*) or one of the diffracted spots (*dark-field diffraction imaging*), see Figure 23. The interactions that form an image with contrast are more complex than presented here, thus requiring analysis of the amplitude of the diffracted and transmitted beams [113].

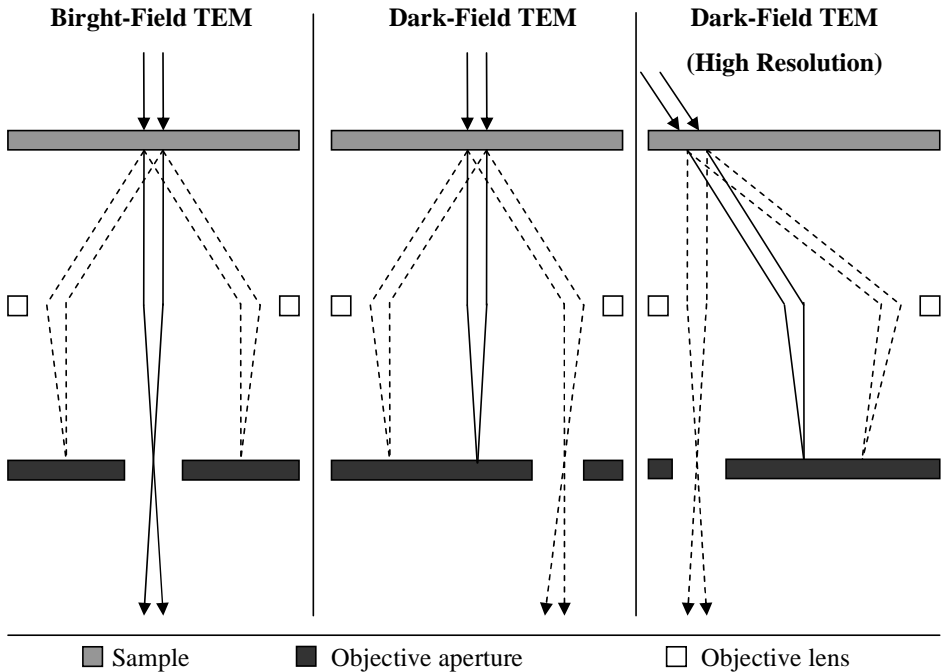


Figure 23: Comparison of bright-field and dark-field imaging [110,112]

Phase contrast imaging

Each scattering event produces a phase shift which is particularly useful to obtain high resolution images at high magnification, this is known as phase contrast imaging. When a beam is scattered, a phase shift of $-\pi/2$ is induced on the scattered beam. The scattered beam then follows a path that differs from the unscattered beam, further increasing the phase shift between the two beams. The path-dependent phase shift is sensitive to many factors such as the specimen thickness, orientation, scattering factor, astigmatism, beam tilt and defocus in the objective lens [110]. Lens aberrations can be used to manipulate further this phase shift by varying the phase for different scattering angles and reciprocal vectors. The unscattered beam will subsequently interfere with the scattered beam that has been affected by these three phase shift phenomena resulting in contrast that is dependent on the spacing of the scattering objects. In order to produce such images, several diffracted beams are required and in general, the more beams included the better the image up to the point where the multitude of beams containing aberrations begin to distort the image again.

The majority of TEM images presented in **Papers 1 – 3** utilise this technique to achieve contrast.

Focussed images

The conditions for best imaging vary widely dependent on sample materials and thickness. While not necessarily the best method for obtaining the best image for small features, Scherzer defocus does provide a general condition for good imaging. A perfect contrast transfer function would feature an overall phase shift of $-\pi$ for scattering objects, such as atoms, and no phase shift where no scattering objects exist. Scherzer defocus is the closest approximation during normal TEM imaging to this perfect contrast transfer function where the aberration function is *almost* uniformly $-\pi/2$ which when combined with the phase shift of the scattering event results in an overall phase shift of $-\pi$, that is, exactly out of phase with the incident beam. This means that scattering objects appear *almost* uniformly dark. A good example of Scherzer defocus and non-Scherzer defocus is found in **Paper 1**, where the defocus was altered significantly from Scherzer defocus in order to image a set of pores at the film interface.

Resolution

A particular configuration of the microscope in terms of aberrations and defocus will lead to a certain phase shift for each scattering object-spacing. This can be described mathematically through the *contrast transfer function*. This function allows calculation of the spacing of scattering objects, which is, in-turn, the correct atomic positions [114,115]. This is the true nature of high-resolution TEM. Note that an approximation has been made here, where (Fresnel) diffraction effects have been ignored; for medium-heavy elements the assumption begins to breakdown after a sample thickness of ~ 3 nm is exceeded [116]. It is clear then, that resolution must be accompanied by the contrast transfer function that specifies the microscope conditions. Different contrast transfer functions will differ in the smallest spacing which information will be obtained. Resolution (or *point resolution*) is defined as being the reciprocal of the highest spatial frequency (or atomic spacing) where the contrast transfer function is approximately equal to -1 . This is *not* equivalent to measuring resolution as the smallest distance of scattering objects that provide information; objects spaced *smaller* than this distance will continue to cause contrast

in the image but the contrast transfer function undulates rapidly at such small spacings making analysis of such contrast mechanisms impractical.

The discussion so far has assumed that the incident beam acts as a parallel, planar wave. This is not the case as the initial electron source is not a point source; beam incoherence and chromatic aberrations dampen the contrast inducing effects and essentially the phase relationships at higher spatial frequencies, smaller distances, are lost [117]. A similar effect is also achieved by increasing the convergence angle of the incident beam [118]. Mathematically, these effects are described by the *information limit*, which represents the limit that information can be transferred by the lenses. This is typically visualised as a damping of the contrast transfer function as shown in Figure 24.

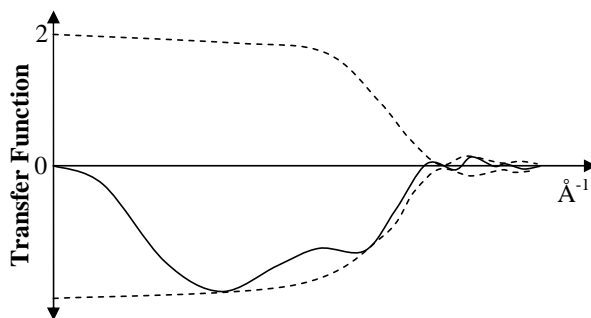


Figure 24: Damped contrast transfer function [110]

Diffraction pattern

Altering the configuration of the lenses in the TEM allows the projection of the back focal plane onto the imaging plane, see Figure 25. The spot pattern obtained is known as the diffraction pattern and can be correlated to the position of the scattering planes within the structure of the material. This pattern provides information regarding the crystal lattice spacings, symmetry, orientation and distribution of grain sizes. Individual areas on the film can be selected through the use of a selected-area aperture, allowing analysis of the diffraction pattern from individual areas. The combination of bright-field TEM image and selected-area electron diffraction pattern provides a wealth of information regarding the structure and as thus are often presented together, see **Papers 1 – 3**. A particular example is shown in **Paper 3**, where XRD analysis showed the monoclinic zirconia phase in the film bulk, but

through the use of selected-area diffraction patterns, the initial nucleation of the tetragonal zirconia phase on the substrate could be identified.

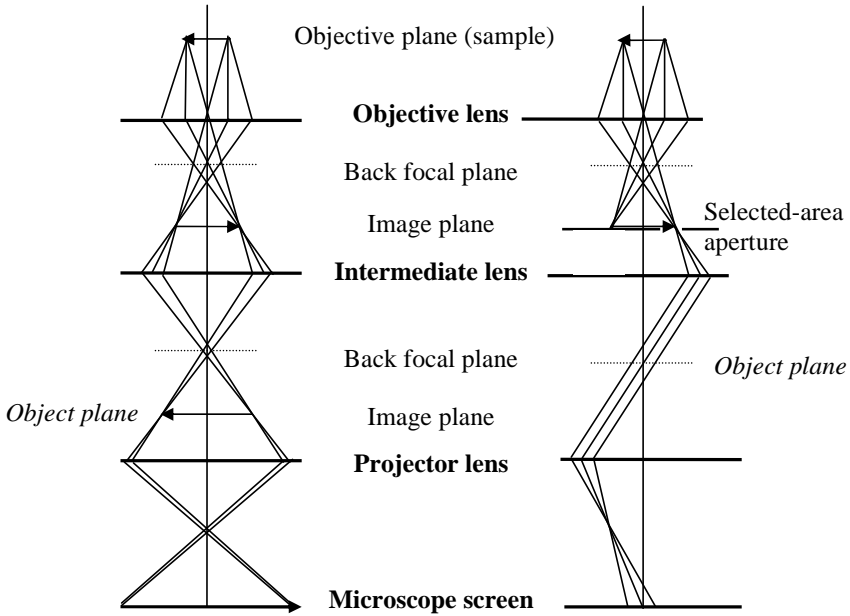


Figure 25: Comparison of imaging mode (left) and diffraction mode (right) [111]

Where the electron beam passes through only one crystal, then a single diffraction pattern arises, see Figure 26. A polycrystalline sample will have multiple grains, that is multiple orientations of the same material, superimposed, resulting in a ring pattern, as often demonstrated in **Paper 1 and 2**. A film preferred orientation will have several patterns superimposed, but with only certain orientations present, hence the presence of arcs in **Paper 3**, rather than full rings.

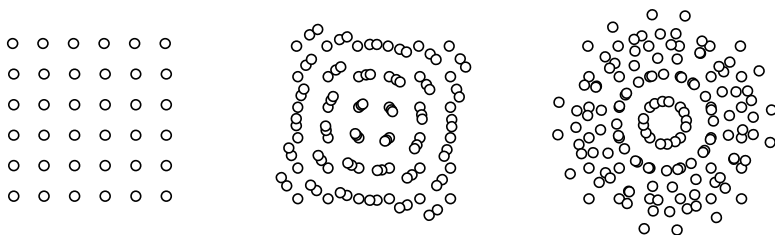


Figure 26: Single crystal diffraction pattern (left) three single crystal diffraction patterns slightly rotated (centre) and five single crystal diffraction patterns (right)

Energy dispersive spectroscopy

The interaction of the electron beam with a sample does not only lead to diffracted electrons, a variety of other emissions occur, see Figure 27. Incident electrons lose energy by knocking out bound electron from the atoms in the specimen, essentially ionising the atoms. These ions are then excited, since they are no longer in their “normal” state. In order to return to their normal state, the atoms release energy in the form of x-rays. These can be collected and analysed since the energy of the x-ray released is characteristic of the excited atom. This method is known as energy dispersive spectroscopy (EDS or EDX) [105]. The wavelength of such x-rays can also be analysed, this being known as wavelength dispersive spectroscopy (WDX).

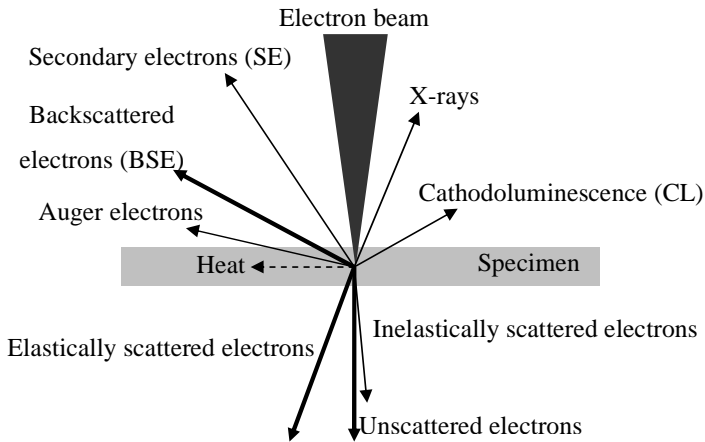


Figure 27: Emissions due to the electron beam [116]

EDX is a convenient analysis technique as the analysis is relatively simple compared to other techniques; standard calibration is performed quickly, in some cases with the use of virtual standards. The method can, however, be quite time consuming since x-rays must be generated from the sample, something that does not occur readily from light elements, and collection angles are poor since the x-ray detector is also located to the side of the sample due to space requirements and the need to accommodate the objective lens pole pieces. This situation is not optimal since x-ray intensity is low parallel to the sample surface [118]. Absorption of x-rays into the sample, large probe sizes compared to the grain sizes, interactions with the substrate, stray x-rays from interactions of the electron beam within the microscope and electron beam broadening within the sample also serve to confuse the analysis. Samples which contain adjacent

elements in the periodic table are not suited to x-ray analysis since the fluorescence of the x-rays affect the analysis of each individual spectrum. These negative factors lead to the use of EDX as a semi-quantitative method in order to gain a rough knowledge of sample composition before proceeding to more complex methods. In **Paper 1** EDX was used to demonstrate the phase separation between alumina and zirconia phases, although full quantification was not performed, for the aforementioned reasons.

Electron energy loss spectroscopy

Electrons that ionise the bounding electrons of the elements in a sample lose energy during the process. These electrons do not, however, deviate significantly from the path of the transmitted beam. A magnetic prism spectrometer located after main imaging lenses can collect the transmitted beam and disperse the electrons according to energy loss, see Figure 28. This is known as electron energy loss spectroscopy or EELS. Since each element in the sample features characteristic ionisation energy, it follows that the energy loss will also be characteristic to an element and can thus be used for characterising the elements within a sample.

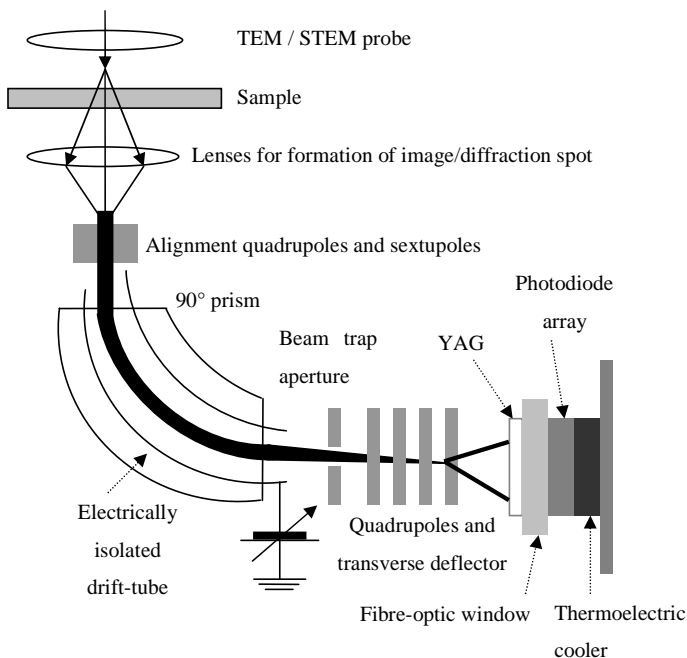


Figure 28: Typical EEL spectrometer configuration for parallel imaging [105,119]

The transmitted beam contains a wealth of information that can be characterised by EELS, see Figure 29 [120,121]. The first feature is the *zero-loss peak*. Most electrons actually pass through a thin specimen without an energy loss. This peak, while not important for spectroscopy, provides information regarding the energy coherency of the electron source, and hence, the energy resolution available in any particular EELS measurement. *Phonons* are present close to the zero-loss peak, these are not usually resolved except in high-resolution reflection mode experiments (HREELS). These can be used in a similar way to other vibrational spectroscopic techniques such as Raman spectroscopy. Following the zero-loss peak is the low-loss region where *plasmons* are typically present. The thicker the sample, the more plasmons present. Each plasmon represents the density of the valence electrons and the width of the rate of decay for a particular mode; this can be calculated from solid-state physics [106]. Shifts in the plasmon peaks also provide indications where valence electrons can be excited to low lying unoccupied electronic states above the Fermi level. In the high-loss region *ionisation edges* are present which correspond to the ionisation of inner shell electrons. In addition to characterisation of the energy loss, the ionisation edge contains information regarding the density of states (DOS), since the unoccupied states near the Fermi level can be modified by the chemical bonding within a solid. This is generally reflected in alterations of the ionisation edge shape 30 – 40 eV from the threshold. This region is known as the *electron energy loss near-edge structure* (ELNES) and provides structure and bonding information. Exact interpretation is quite difficult, but can be aided through electronic structure calculations that model the density of states for a particular material. Beyond this region the *extended energy loss fine structure* (EXELFS) contains information regarding the bond distances and coordination of atoms. Finally, the *Compton profile* results from large scattering angles where the electrons are essentially hard spheres, the width of this feature can also provide information regarding bonding, although it is rarely used. In this study, the ionisation edges of particular elements in different samples have been investigated, the differences in structure are evident in **Paper 2**.

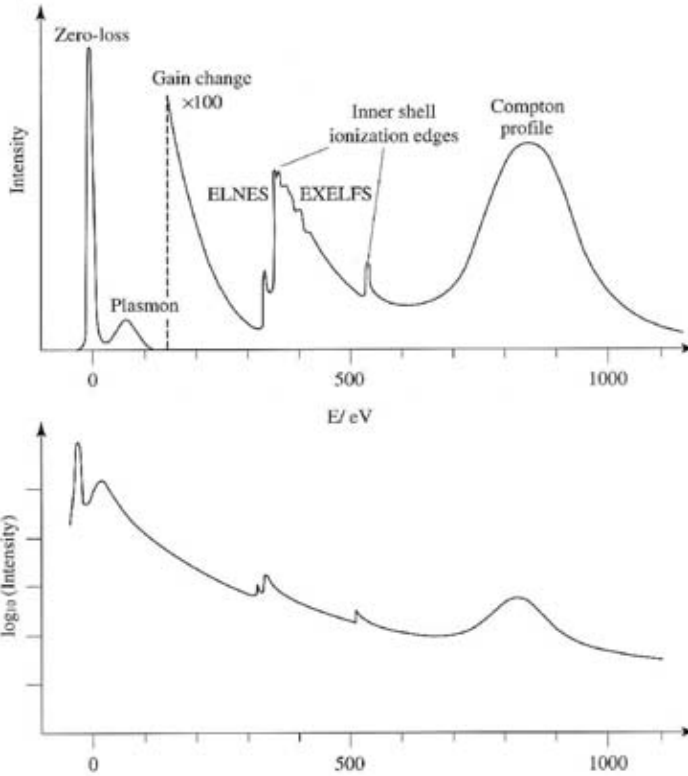


Figure 29: Typical linear (top) and logarithmic (bottom) EEL spectra [120]

It must be noted that while a thicker specimen results in more inelastically scattered electrons, more plasmons also result and the spectrum becomes confused due to convolution between plasmons and edges. In practice, a thin area ($<1 - 0.5 \lambda$) [105,119] for viewing is almost always desired.

Scanning transmission electron microscopy

The electron beam may be focussed into an atomic sized probe, rather than the parallel illumination typical in TEM. This atomic-sized probe may then be scanned across a sample; information comes only from the area where the probe is scanning. At each point, a diffraction pattern is formed. This pattern can be collected and an image can be constructed by taking the intensity of the scattered rays for each particular point, or pixel that is scanned, this method is known as scanning transmission electron microscopy (STEM) [110]. A comparison between STEM and conventional TEM is given below in Figure 30.

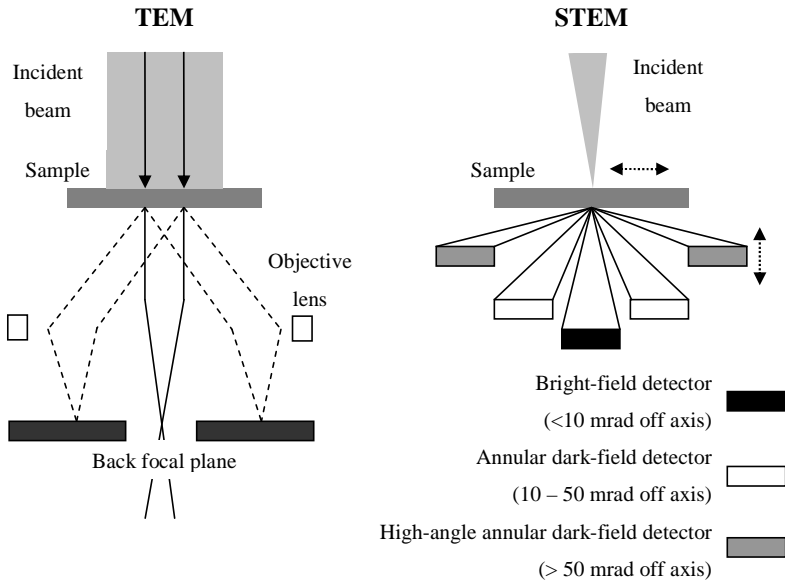


Figure 30: Schematic of the layout of STEM in comparison to TEM [110]

Imaging is possible on a scale much finer than available from TEM with a parallel beam; the lenses are not directly involved in the formation of the image after the electron beam has interacted with the sample and as such objective lens aberrations do not directly affect the quality of the image^{**}. Magnification is achieved by scanning a smaller area with more points, or pixels. Resolution must be redefined in this case as being related to the interaction area of the electron probe, this is mainly dependent on the electron source and the size of the probe formed mainly using the condenser, but also the objective lenses. Here, the elimination of lens aberrations is extremely important to the formation of the smallest imaging probe possible. Analysis techniques such as EDX and EELS remain compatible with STEM, and are even enhanced by the ability to restrict the area where information is obtained to sub-nanometre resolution and precision.

Imaging is also time consuming compared to normal TEM imaging since the electrons are used less efficiently [122]. The best information for mass-thickness contrast is typically provided from large diffraction angles, but at these angles the scattered

^{**} Objective lens aberrations do, however, affect probe formation, and hence, indirectly affect the quality of the image.

intensity is quite low. This technique is demonstrated in **Paper 1** where *in-situ* EDX analysis showed phase separation on a scale of a few nanometres.

Ion Beam Techniques

Rutherford backscattering spectrometry

Rutherford backscattering spectrometry (RBS) involves a beam of highly-energetic light ions, typically hydrogen or helium, directed toward the surface of a sample at near-normal angles. The ions will penetrate deep into the surface of the material, generating elastic collisions with the atoms within the sample, these collisions lead to backscattering of the incident ions, see Figure 31. The energy of the scattered ions can be related to the mass of the atom in the sample, through the conservation of momentum [72,123]. The collision itself is insensitive to the electronic configuration or chemical bonding of the atoms in the material; it is sensitive only to relative masses and energies. The energies of the backscattered ions can be expressed in-principle by Equation 10, giving the mass of the atoms present in the sample. Analysis becomes naturally more complex when the scattering cross-section and energy loss prior to the scattering are considered, these parameters are generally used when depth profiling or calculating concentrations. Since this is a first principles calculation, no elemental standards are required for the chemical analysis. In order to analyse the data, a simulation is made of a hypothetical material with a particular composition and depth profile. This is then compared to the measured spectra. In this work, simulations were created using the SIMNRA 5.0 code that incorporates stopping powers for various ions published by Andersen-Ziegler [123 – 125]. This process involves iterative fitting and it is important that other measurement techniques are also used to estimate the composition and film thickness since it is easy to confuse elements. An example from this study: Tantalum can be easily confused with hafnium, which appears as an impurity in zirconium targets and hence zirconia films. RBS was used in **Paper 1** and **Paper 2** for the analysis of the ratio of metal atoms in the films. When these measurements were combined with other ion beam techniques, a full picture of the stoichiometry could be obtained; leading to a hypothesis that oxygen under-stoichiometry is an important factor in the stabilisation of the cubic zirconia phase in the nanocomposites.

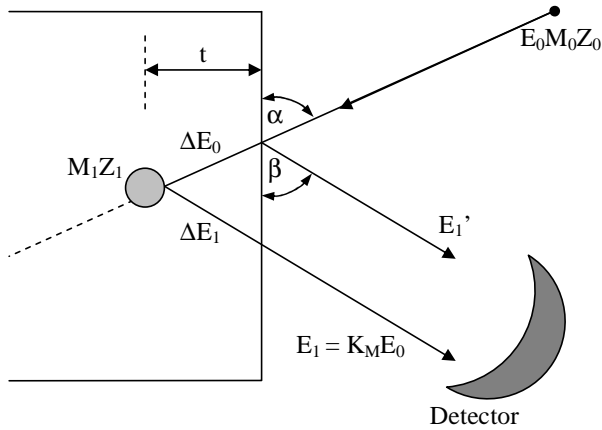


Figure 31: Schematic of Rutherford backscattering [123]

$$E_1 = \left\{ \frac{(M^2 - M_0^2 \sin^2 \theta)^{1/2} + M_0 \cos \theta}{M_0 + M} \right\}^2 E_0 = K_M E_0 \quad \text{Equation 10 [123]}$$

- Where:
- E_1 – Energy of backscattered ions
 - E_0 – Energy of incident ion
 - M – Mass of atom in material
 - M_0 – Mass of incident ion
 - θ – Scattering angle
 - K_M – Kinematic factor

Elastic recoil detection analysis

Light elements do not readily backscatter other atoms, at least not with energies sufficient for detection. This is clearly seen by placing a small mass for M in Equation 10. The mechanics of particle collisions is, however, changed if the beam is incident at an angle. In this case, light atoms are more likely to be ejected from the sample (recoiling), while the heavy incident atoms can also be forward scattered into a path roughly similar to the recoiled light atoms, see Figure 32. The energies of the recoiled atoms are again related to the mass of a particular species based on collision kinematics [123]. Depth profiling is also possible by approximating the surface energy and the stopping power of particular ions. Electron recoil detection analysis (ERDA) is able to detect hydrogen, an element that is typically quite difficult to detect with other methods given the low mass of the hydrogen atom. ERDA measurements

were used to investigate the theory that oxygen under-stoichiometry was responsible for the formation of metastable zirconia phases as presented in **Paper 1** and **Paper 2**. Since aluminium is a relatively light metal, the ERDA measurement of the aluminium was normalised with the RBS measurement of the same metal. In this way, both heavy elements and light elements could be quantified. It should be noted that while RBS is suited to heavier elements, and ERDA is suited to lighter elements, it is possible to make measurements of the “unsuitable” elements with both techniques. It was found that the variation between RBS and ERDA in the case of aluminium, zirconium and oxygen were not tremendous (> 2 at.%). It may have sufficed to use one technique only, but by normalising the result, greater accuracy is achieved.

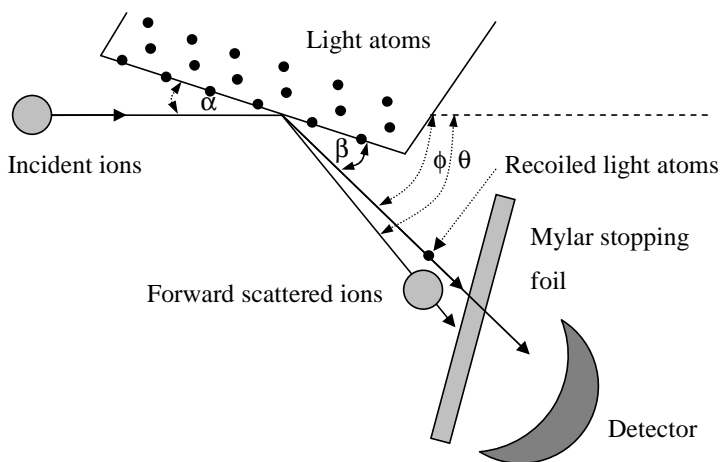


Figure 32: Schematic of elastic recoil detection analysis [123]

X-Ray Photoelectron Spectroscopy

X-ray photons incident on a sample surface cause the atoms near the surface to eject core and valence level electrons [126], see Figure 33. The kinetic energy of the electron corresponds to the initial energy of the x-ray photon minus the energy required to remove the electron, being the characteristic binding energy and the work function [127], see Equation 11. By collecting the electrons in a hemispherical analyser and measuring their kinetic energy, the elements present on the surface of a material can be characterised. This technique is known as x-ray photoelectron spectroscopy (XPS). The information provided is not, however, limited to which atoms that are present, the technique also provides information about the chemical

environment which the atoms are present since the binding energies of atoms of the same element can still vary due to differences in formal oxidation state, molecular environment, valence electron density and core electron shielding [127]. For example, zirconium atoms that are bonded to an electronegative element, such as oxygen, will exhibit a slightly higher binding energy compared to zirconium atoms bonded to metallic elements, such as other zirconium atoms, even when the same core level electrons are examined.

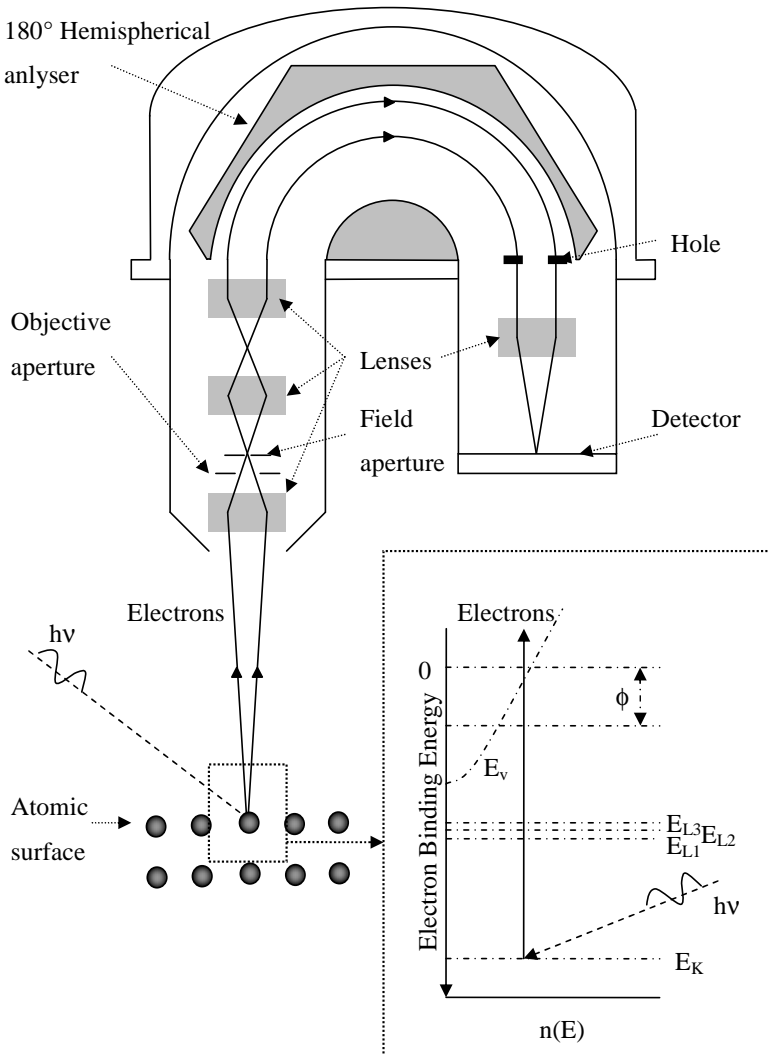


Figure 33: Schematic of XPS measurement apparatus and (inset) electron energy diagram showing the XPS process [126,127]

$$E_K = h\nu - E_B - e\phi \quad \text{Equation 11 [127]}$$

Where:

- E_K – Kinetic energy of ejected photoelectron
- E_B – Core level binding energy
- $e\phi$ – Work function
- $h\nu$ – Characteristic energy of X-ray photon

Quantification of the XPS spectra requires calibration of the energy dependence of the intensity/energy response of a particular spectrometer [128]. This is achieved through the measurement of standard reference compounds and calculating the appropriate sensitivity factors to allow proper background subtraction. The peak areas may then be related to the relative amount of each element in the material. The binding energy scale is also calibrated from elements of high purity where the energy is well-defined, such as gold and copper. To obtain a depth profile, an argon beam is used to sputter the material effectively allowing information from a greater depth. The problem with sputtering is, however, that different atoms sputter preferentially [127], leading to inaccuracies. This technique was utilised in **Paper 3**, where the intensities of the peaks for each element were measured and then correlated to the amount of material in the film. Indications on whether the metals were bonded to oxygen only, as in a stoichiometric film, or were bonded to other metals, as in an oxygen-deficient film were also obtained.

Summary and Contribution to the Field

“If we do not forget, then the world is soon nothing but a gigantic library”

John Coetzee: *The Master from St Petersburg*

Alumina-zirconia thin films were produced by different sputter deposition methods, including from ceramic and metallic targets, with two types of power sources, leading to a range of possible plasma conditions. **Paper 1** is the first report of alumina-zirconia sputtered films that are nanocrystalline *without* post-deposition heat treatment or special, multilayer structures. The growth of such films was achieved at a relatively low substrate temperature, ~450 °C. The films deposited in that particular part of this study were, however, limited to the zirconia rich part of the quasi-binary phase diagram. In **Paper 2**, composites in the alumina-rich part of the phase diagram were also synthesised. In addition, the electron energy loss spectra for the composites were reported. The films in **Paper 1** and **Paper 2** were deposited with RF magnetron sputtering. Further results from DC magnetron sputtering in **Paper 3** pushed the already low temperatures for the formation of crystalline phases even further down, to ~300 °C, opening new possibilities for substrate materials. In addition, the growth rate for the films was increased markedly, demonstrating that such films are achievable in industrial pilot-plant scale systems.

In **Papers 1 – 3**, the monoclinic zirconia phase was formed films of pure zirconia. Crystalline preferred orientation in the <100> directions was present in **Paper 3**. Two metastable zirconia structures have also been synthesised. In **Paper 1**, the cubic zirconia phase was deposited. The suggested mechanisms for the formation of this cubic polytype phase have been alumina segregation from the grains causing lattice restraint and oxygen deficiency in the zirconia phase. In **Paper 2**, this hypothesis was tested by increasing the oxygen partial-pressure. Here, the cubic zirconia formed, but required higher substrate temperatures. The γ -alumina phase was also deposited, this phase has long been of interest as a possible wear-resistant coating [51]. The metastable tetragonal zirconia phase was achieved in **Paper 3**; the suggested mechanism being further reduction in adatom mobility by change of the power supply and hence change in the energy of the particles in the plasma.

The process involved in the formation of these novel structures has been studied in **Papers 4 and 5**. In **Paper 4**, the transport phenomenon of particles across the plasma has been studied by modelling the flow of reactive species. The resultant model is capable of describing reactive sputtering from two targets in a dual-gas environment, building on the previous models [80]. In **Paper 5**, the actual deposition flux from various sources has been analysed and the energy distributions coupled to the formation of individual phases. The role of metal-oxide ionic clusters, such as AlO^+ and ZrO^+ to the stoichiometry of the final film has been highlighted. In addition, the energy distribution of ions has been reported for alumina and zirconia.

These results presented here show that a range of metastable zirconia and alumina phases can be controllably deposited by magnetron sputtering. Through the parameters available in a sputtering system, the structures and properties of a nanocomposite can also be tailored.

Future Outlook

“but yet it is not the last stroke that fells the tree,
nor the last word nor gaspe that qualifies the soule.”
John Donne: *Deaths Duell*

Alumina-zirconia nanocomposite films with a range of metastable phases and novel microstructures can be fabricated through magnetron sputtering. Further understanding of the mechanisms that underlie the formation of various crystalline phases would allow tailoring the microstructure to specific needs. *A functional ceramic in the alumina-zirconia system would result.* To understand the mechanisms of formation, studies of the effects of the substrate bias as a deposition parameter are required.

In tailoring the microstructure a full range of compositions should be achieved. As compositions close to 50:50 alumina:zirconia are currently amorphous, more work must be directed in the formation of crystalline phases, without promoting additional reaction with the substrate. Again, this points toward a study of substrate bias effects on the growth of alumina-zirconia nanocomposites. Altering the flux of particles to an ionised flow, such as with high-powered impulse magnetron sputtering (HiPIMS) would also be a possible avenue of study.

Density functional theory modelling of the zirconia and alumina structures will also aid in the understanding why some phases form under reactive sputtering conditions, while other phases do not form. Such studies will also contribute to the interpretation of the EEL spectra since it would be possible to describe the density of states present in the ELNES. Future characterisation techniques will also elucidate whether the current indications that alumina separates at the grain boundaries in the nanocomposite are correct.

Preliminary results, not included in this thesis, indicate that vibrational spectroscopy techniques, such as Raman scattering, can be used for phase identification and further characterisation of alumina-zirconia nanocomposites. The initial study was performed on the films produced in **Paper 1**, which were limited in thickness. Since thicker films are now possible, vibrational spectroscopy should be revisited.

Having developed nanocomposite alumina-zirconia nanocomposite thin films, the applicability of such nanocomposites should be examined. Similar composites have proved successful in bulk ceramics and in cutting tool applications [67,68] but in order to apply thin films to these applications, the pores between the columns must be removed. Once again, substrate bias may play a role in avoiding the formation of pores. With a denser film, mechanical testing, such as nanoindentation, can characterise the performance of these films.

References

- [1] E. Lutz, M. Swain and N. Claussen: "Thermal shock behavior of duplex ceramics" *Journal of the American Ceramic Society* **74** [1] (1991) 19 – 24
- [2] *Modern Metal Cutting: A Practical Handbook*, AB Sandvik Coromant, Sandviken, Sweden (1994) ISBN 91-972299-0-3
- [3] J. Müller, M. Schierling, E. Zimmerman, and D. Neuschütz: "Chemical vapor deposition of smooth α -Al₂O₃ films on nickel base superalloys as diffusion barriers" *Surface and Coatings Technology* **120** – **1** (1999) 16 – 21
- [4] Y Su, H. Wang, W. Porter, A. De Arellano Lopez and K. Faber: "Thermal conductivity and phase evolution of plasma sprayed multilayer coatings" *Journal of Materials Science* **36** (2001) 3511 – 8
- [5] M. Voigt and M. Sokolowski: "Electrical properties of thin RF sputtered aluminum oxide films" *Materials Science and Engineering B* **109** (2004) 99 – 103
- [6] J. Gole, S. Prokes, J. Stout, O. Glembocki and R. Yang: "Unique properties of selectively formed zirconia nanostructures" *Advanced Materials* **18** (2006) 664 – 7
- [7] *Alumina as a Ceramic Material*, W. Gitzen [Ed], American Ceramic Society, Westerville, Ohio, USA (1970) ISBN: 0-916094-46-4
- [8] R. Stevens: *Introduction to Zirconia*, Magnesium Elektron Ltd. (1986)
- [9] J. Schneider, W. Sproul and A. Matthews: "Phase formation and mechanical properties of alumina coatings prepared at substrate temperatures less than 500°C by ionized and conventional sputtering" *Surface and Coatings Technology* **94-5** (1997) 179 – 83
- [10] W. Sproul, D. Christie and D. Carter: "Control of reactive sputtering processes" *Thin Solid Films* **491** (2005) 1 – 17
- [11] Z. Ji and J. Rigsbee: "Growth of tetragonal zirconia coatings by reactive sputter deposition" *Journal of the American Ceramic Society* **84** [12] (2001) 2841 – 4
- [12] T. Jung and A. Westphal: "Zirconia thin film deposition on silicon by reactive gas flow sputtering: The influence of low energy particle bombardment" *Materials Science and Engineering A* **140** (1991) 528 – 33
- [13] D. Ruddell, B. Stoner and J. Thompson: "The effect of deposition parameters on the properties of yttria-stabilized zirconia thin films" *Thin Solid Films* **445** (2003) 14 – 9
- [14] S. Spiro, S. Guicciardi, A. Belloso, G. Pezzotti: "Yttria-stabilized zirconia films grown by radiofrequency magnetron sputtering: Structure, properties and residual stress" *Surface and Coatings Technology* **200** (2006) 4579 – 4585
- [15] C. Aita, M. Wiggins, R. Whig and C. Scanlan: "Thermodynamics of tetragonal zirconia formation in a nanolaminate film" *Journal of Applied Physics* **79** [2] (1996) 1176 – 8
- [16] M. Schofield, C. Aita, P. Rice and M. Gajdardziska-Josifovska: "Transmission electron microscopy study of zirconia-alumina nanolaminates grown by reactive sputter deposition. Part I: Zirconia nanocrystallite growth morphology" *Thin Solid Films* **326** (1998) 106 – 16
- [17] S. Qadri, C. Gilmore, C. Quinn, E. Skelton and C. Gossett: "Phase stability of ZrO₂-Al₂O₃ thin films deposited by magnetron sputtering" *Physical Review B* **39** [9] (1989) 6234 – 7
- [18] C. Gilmore, C. Quinn, E. Skelton, C. Gossett and S. Qadri: "Stabilized zirconia-alumina thin films" *Journal of Vacuum Science and Technology A* **4** [6] (1986) 2598 – 600
- [19] G. Orange, G. Fantozzi, F. Cambier, C. Leblud, M.R. Anseau, A. Leriche: "High temperature mechanical properties of reaction sintered mullite/zirconia and mullite/alumina/zirconia composites" *Journal of Materials Science* **20** (1985) 2533 – 40
- [20] G. Aneziris, E. Pfaff, H. Maier: "Corrosion mechanisms of low porosity ZrO₂ based materials during near net shape steel casting" *Journal of the European Ceramic Society* **20** (2000) 159 – 65
- [21] D. Clarke, C. Levi and A. Evans: "Enhanced zirconia thermal barrier coating systems" *Journal of Power and Energy A* **220** [1] (2006) 85 – 92
- [22] R. Hannink, P. Kelly and B. Muddle: "Transformation toughening in zirconia-containing ceramics" *Journal of the American Ceramic Society* **83** [3] (2000) 461 – 87
- [23] G. Garvie, R.H.J. Hannink, R. Pascoe: "Ceramic steel?" *Nature* **258** (1975) 703 – 4
- [24] *Binary Alloy Phase Diagrams*, T. Massalski, J. Murray, L. Bennett and H. Baker [Eds.], American Society for Metals, Metals Park, Ohio, USA (1986) ISBN 0-87180-262-4
- [25] X. Zhao and D. Vanderbilt: "Phonons and lattice dielectric properties of zirconia", *Physical Review B* **65** (2002) 075105

- [26] M. Fèvre, A. Finel and R. Caudron: "Local order and thermal conductivity in yttria-stabilized zirconia. I. Microstructural investigations using neutral diffuse scattering and atomic-scale simulations" *Physical Review B* **72** [10] (2005) 104117
- [27] A. Foster, V. Sulimov, F. Gejo, A. Shluger and R. Nieminen: "Structure and electrical levels of point defects in monoclinic zirconia" *Physical Review B* **64** (2001) 224108
- [28] I. Nettlehip, R. Stevens: "Tetragonal zirconia polycrystal (TZP) – A review" *International Journal of High Technology Ceramics* **3** [1] (1987) 1 – 32
- [29] F. Lange: "Transformation toughening: Part 1, size effects associated with thermodynamics of constrained transformations" *Journal of Materials Science* **17** (1982) 225 – 34
- [30] F. Lange: "Transformation toughening: Part 4, fabrication, fracture toughness and strength of Al_2O_3 - ZrO_2 composites" *Journal of Materials Science* **17** (1982) 247 – 54
- [31] R. Garvie: "The occurrence of tetragonal zirconia as a crystallite size effect" *Journal of Physical Chemistry* **69** [4] 1238 – 43
- [32] T. Mitsuhashi, M. Ichihara and U. Taksuke: "Characterization and stabilization of metastable tetragonal ZrO_2 " *Journal of the American Ceramic Society* **57** [2] (1974) 97 – 101
- [33] S. Ben Amor, B. Roiger, G. Baud, M. Jacquet and M. Nardin: "Characterization of zirconia films deposited by R.F. magnetron sputtering" *Materials Science and Engineering B* **57** (1998) 28 – 39
- [34] K. Muraleedharan, J. Subrahmanyam and S. Bhaduri: "Identification of t' phase in ZrO_2 -7.5wt% Y_2O_3 thermal-barrier coatings" *Journal of the American Ceramic Society Communications* **71** [5] (1988) C226 – 7 s
- [35] N. Robello, A. Gandhi and C. Levi: "Phase stability issues in emerging TBC systems" *High Temperature Corrosion and Materials Chemistry IV*, E. Opila, P. Hou, T. Maruyama, B. Pieraggi, M. McNallan, D. Shifler and E. Wuchina [Eds.] *Electrochemical Society Proceedings* **PV2003-16** (2003) 431 – 42
- [36] L. Lenz and A. Heuer: "Stress-induced transformation during subcritical crack growth in partially stabilized zirconia" *Journal of the American Ceramic Society Communications* **65** [11] (1982) C192 – 3
- [37] I. Levin and D. Brandon: "Metastable alumina polymorphs: Crystal structures and transition sequences" *Journal of the American Ceramic Society* **81** [8] (1998) 1995 – 2012
- [38] H. Pinto, R. Nieminen and S. Elliott: "Ab initio study of γ - Al_2O_3 surfaces" *Physical Review B* **70** (2004) 125402
- [39] R.-S. Zhou and R. Snyder: "Structures and transformation mechanisms of the η , γ and θ transition aluminas" *Acta Crystallographica B* **47** (1991) 617 – 30
- [40] *International Tables for X-Ray Crystallography*, M. Buerger, C. MacGillavry, N. Henry, J. Kasper and K. Lonsdale [Eds.], The International Union of Crystallography, 3rd Edition (1969)
- [41] R. Ahuja, J. Osorio-Guillen, J. Souza de Almeida, B. Holm, W. Ching and B. Johansson: "Electronic and optical properties of γ - Al_2O_3 from ab initio theory" *Journal of Physics: Condensed Matter* **16** (2004) 2891 – 900
- [42] "Alumina crystal structures", M. Halvarsson, <http://fy.chalmers.se/~f10mh/CVD/aluminaintro.html>, last updated April 22, 2002
- [43] Y. Yourdshahyan, C. Ruberto, M. Halvarsson, L. Bengtsson, V. Langer, B. Lundqvist, S. Rupp and U. Rolander: "Theoretical structure determination of a complex material: κ - Al_2O_3 " *Journal of the American Ceramic Society* **82** [6] (1999) 1365 – 80
- [44] P. Liu and J. Skogsmo: "Space-group determination and structure model for κ - Al_2O_3 by convergent beam electron diffraction (CBED)" *Acta Crystallographica B* **47** (1991) 425 – 33
- [45] J. Skogsmo, M. Halvarsson and S. Vuorinen: "Microstructural study of the κ - $\text{Al}_2\text{O}_3 \rightarrow \alpha$ - Al_2O_3 transformation in CVD κ - Al_2O_3 " *Surface and Coatings Technology* **54 – 5** (1992) 186 – 92
- [46] G. Gutiérrez, A. Taga and B. Johansson: "Theoretical structure determination of γ - Al_2O_3 " *Physical Review B* **65** (2001) 012101
- [47] G. Paglia: "Determination of the structure of γ -Alumina using empirical and first principles calculations combined with supporting experiments" PhD Thesis, Curtin University, Australia (2004)
- [48] K. Sohlberg, S. Pennycook and S. Pantelides: "The bulk and surface structure of γ -alumina" *Chemical Engineering Communications* **181** (2000) 107 – 138
- [49] C. Tanner, M. Sawkar-Mathur, J. Lu, H.-O. Blom, M. Toney and J. Chang: "Structural properties of epitaxial γ - Al_2O_3 (111) thin films on 4H-SiC (0001)" *Applied Physics Letters* **90** [6] (2007) 061916
- [50] M.-H. Lee, C.F. Cheng, V. Heine and J. Klinowski "Distribution of tetrahedral and octahedral Al sites in gamma alumina" *Chemical Physics Letters* **265** (1997) 673 – 6
- [51] M. Åstrand, T. Selinder, F. Fietzke and H. Klostermann: "PVD- Al_2O_3 coated cemented carbide cutting tools", *Surface and Coatings Technology* **188 – 9** (2004) 186 – 92

- [52] H. Klostermann, B. Böcher, F. Fietzke, T. Modes and O. Zywitzki: "Nanocomposite oxide and nitride hard coatings produced by pulsed magnetron sputtering" *Surface and Coatings Technology* **200** (2005) 760 – 4
- [53] J. McHale, A. Aurox, A. Perrotta and A. Navrotsky: "Surface energies and thermodynamic phase stability in nanocrystalline aluminas" *Science* **277** (1997) 788 – 91
- [54] C. Ruberto, Y. Yourdshahyan and B. Lundqvist: "Surface properties of metastable alumina: A comparative study of κ - and α -Al₂O₃" *Physical Review B* **67** (2003) 195412
- [55] H. Pinto, R. Nieminen and S. Elliott: "Ab initio study of γ -Al₂O₃ Surfaces" *Physical Review B* **70** (2004) 125402
- [56] M. Macêdo, C. Bertan and C. Osawa: "Kinetics of the $\gamma \rightarrow \alpha$ Alumina phase transformation by quantitative X-ray diffraction" *Journal of Materials Science* **42** [9] (2007) 2830 – 6
- [57] C. Ruberto: "Metastable alumina from theory: Bulk, surface, and growth of κ -Al₂O₃" PhD Thesis, Chalmers University of Technology, Sweden (2001) ISBN: 91-7291-054-2
- [58] K. Wefers and C. Misra, Alcoa Technical Paper No 19, Alcoa Laboratories, Pittsburg, PA, USA (1987)
- [59] J. Schneider, W. Sproul, A. Voevodin and A. Matthews: "Crystalline alumina deposited at low temperatures by ionized magnetron sputtering" *Journal of Vacuum Science and Technology A* **12** [2] (1997) 1084 – 8
- [60] J. Kuntz, G.-D. Zhan and A. Mukhejee: "Nanocrystalline-matrix ceramic composites for improved fracture toughness" *Materials Research Society Bulletin* **29** [1] (2006) 22 – 7
- [61] D. Rutman, Yu. Toropov, S. Pliner, A. Neumin, Yu. Polejaev: *Viskoogneuporni Materiali iz Dioksida Zirconia (Metallurgia)* (1985) {Д. Рутман, Ю. Торопов, С. Плинер, А. Неумин, Ю. Полежаев: Высокоогнеупорные Материалы из Диоксида Циркония <<Металлургия>>}
- [62] O. Fabricznaya and F. Aldinger: "Assessment of thermodynamic parameters in the system ZrO₂-Y₂O₃-Al₂O₃" *Zeitschrift Für Metallkunde* **95** (2004) 27 – 39
- [63] D. Jerebtsov, G. Mikhailov and S. Sverdina: "Phase diagram of the system Al₂O₃-ZrO₂" *Ceramics International* **26** (2000) 821 – 3
- [64] M. Leverkoehne, R. Janssen, C. Claussen: "Phase development of Zr_xAl_y-Al₂O₃ composites during reaction sintering of Al/ZrO₂/Al₂O₃ powder mixtures" *Journal of Materials Science Letters* **21** [2] (2002) 179 – 83
- [65] E. Hall: "The deformation and ageing of mild steel: III Discussion of results" *Proceedings of the Physical Society B* **64** [9] (1951) 747 – 53
- [66] N. Petch: "The cleavage strength of polycrystals" *Journal of the Iron and Steel Institute* **174** (1953) 25 – 8
- [67] V. Sergio, V. Lughì, G. Pezotti, E. Lucchi, S. Meriani, N. Muraki, G. Katagiri, S. Lo Casto and T. Nishida: "The effect of wear on the tetragonal-to-monoclinic transformation and the residual stress distribution in zirconia-toughened alumina cutting Tools" *Wear* **214** (1998) 264 – 70
- [68] S. Lo Casto, E. Lo Valvo, E. Lucchini, S. Maschio, M. Piacentini and V. Ruisi: "Machining of steel with advanced ceramic cutting tools" *Key Engineering Materials* **114** (1996) 105 – 34
- [69] S. Sharafat, A. Kobayashi, Y. Chen and N. Ghoniem: "Plasma spraying of micro-composite thermal barrier coatings" *Vacuum* **65** (2002) 415 – 25
- [70] M. Lieberman and A. Lichtenberg: *Principles of Plasma Discharges and Materials Processing*, 2nd Edition, John Wiley & Sons, New Jersey, USA (2005) ISBN 0-471-72001-1
- [71] F. Chen: *Introduction to Plasma Physics and Controlled Fusion – Volume 1: Plasma Physics*, 2nd Edition, Plenum Press, New York, USA (1984) ISBN 0-306-41332-9
- [72] M. Ohring: *Materials Science of Thin Films: Deposition and Structure* 2nd Edition, Academic Press, London, UK (2002) ISBN: 0-12-524975-6
- [73] B. Chapman: *Glow Discharge Processes – sputtering and plasma etching*, John Wiley & Sons, New York, USA (1980) ISBN 0-471-07828-X
- [74] D. Mattox: "Particle bombardment effects on thin-film deposition: A Review" *Journal of Vacuum Science and Technology A*, **7** [3] 1105 – 14 (1989)
- [75] K. Wasa, M. Kitabatake and H. Adachi: *Thin Film Materials Technology: Sputtering of Compound Materials*, William Andrew Publishing, Norwich, NY, USA (2004) ISBN: 0-8155-1483-2
- [76] S. Swann: "Magnetron sputtering" *Physics in Technology* **19** [2] (1988) 67 – 75
- [77] I. Safi: "Recent aspects concerning DC reactive magnetron sputtering of thin films: A Review" *Surface and Coatings Technology* **127** (2000) 203 – 19
- [78] S. Schiller, U. Heisig, K. Goedicke, K. Schade, G. Teschner and J. Henneberger: "Advances in high rate sputtering with magnetron-plasmatron processing and instrumentation" *Thin Solid Films* **64** [3] (1979) 455 – 67

- [79] S. Schiller, U. Heisig, K. Steinfeld, J. Strümpfel and W. Sieber: "Reactive D.C. high-rate sputtering with magnetron/plasmatron for industrial applications" *Vakuum-Technik* **30** [1] 1980 3 – 14
- [80] S. Berg and T. Nyberg: "Fundamental understanding and modeling of reactive sputtering processes" *Thin Solid Films* **476** (2004) 215 – 23
- [81] S. Berg, H.-O. Blom, T. Larsson and C. Nender: "Modeling of reactive sputtering of compound materials" *Journal of Vacuum Science and Technology A* **5** [2] (1987) 202 – 7
- [82] S. Berg, H.-O. Blom, M. Moradi, C. Nender and T. Larsson: "Process modeling of reactive sputtering" *Journal of Vacuum Science and Technology A* **7** [3] (1989) 1225 – 9
- [83] S. Venkataraj, O. Kappertz, R. Jayavel, M. Wuttig: "Growth and characterization of zirconium oxynitride films prepared by reactive direct current magnetron sputtering" *Journal of Applied Physics* **92** [5] (2002) 2461 – 6
- [84] K. Ellmer: "Magnetron sputtering of transparent conductive zinc oxide: relation between the sputtering parameters and the electronic properties" *Journal of Physics D: Applied Physics* **33** [4] (2000) R17 – R32
- [85] J. Szczyrbowski, G. Teschner and J. Bruch: "Apparatus for depositing thin layers on a substrate", European Patent EP0795623A1 (1997) {"Vorrichtung zum Aufbringen dünner Schichten auf ein Substrat" Offenlegungsschrift DE19609970}
- [86] E. Kawamura, V. Vahedi, M. Lieberman and C. Birdsall: "Ion energy distributions in rf sheath; review, analysis and simulation" *Plasma Sources Science and Technology* **8** (1999) R45 – R64
- [87] J. Coburn and E. Kay: "Positive-ion bombardment of substrates in rf diode glow discharge sputtering" *Journal of Applied Physics* **43** [12] (1972) 4965 – 71
- [88] H. M. Mott-Smith and I. Langmuir: "The theory of collectors in gaseous discharges", *Physical Review* **28** (1926) 727 – 63
- [89] M. Nisha, K. J. Saji, R. S. Ajimsha, N. V. Joshy and M. K. Jayaraj: "Characterization of radio-frequency plasma using Langmuir probe and optical emission spectroscopy" *Journal of Applied Physics* **99** (2006) 033304
- [90] D. Maundrill, J. Slatter, A. I. Spiers and C. C. Welch: "Electrical measurements of RF-generated plasmas using a driven electrostatic probe technique" *Journal of Applied Physics D: Applied Physics* **20** (1987) 815 – 9
- [91] T. I. Cox, V. G. Deshmukh, D. A. O. Hope, A. J. Hydes, N. ST Braithwaite and N. M. P. Benjamin: "The use of Langmuir probes and optical emission spectroscopy to measure electron energy distribution functions in RF-generated argon plasmas" *Journal of Physics D: Applied Physics* **20** (1987) 820 – 4
- [92] F. Shunoki and A. Itoh: "Mass spectrometric analysis in RF reactive sputtering discharge" *Japanese Journal of Applied Physics Supplement* **2** [1] (1974) 505 – 8
- [93] A. Palermo, E. van Hattum, W. Arnoldbrik, A. Vredenberg and F. Habraken: "Characterization of the plasma in a radio-frequency magnetron sputtering system" *Journal of Applied Physics* **95** [12] (2004) 7611 – 8
- [94] J. Rosén: "Theoretical and experimental studies related to the compositional and microstructural evolution of alumina thin films" PhD Thesis, Rheinisch-Westfälischen Technischen Hochschule Aachen, Germany (2004)
- [95] Plasma Process Monitor (PPM 422) Handbook, Pfeiffer Vacuum (2003)
- [96] J. Thornton: "The microstructure of sputter-deposited coatings" *Journal of Vacuum Science and Technology A* **4** [6] (1986) 3059 – 65
- [97] B. Movchan and A. Demchishin: "Study of the structure and properties of thick vacuum condensates of nickel, titanium, tungsten, aluminium oxide and zirconium dioxide" *Physics of Metals and Metallography* **28** (1969) 83 – 90 {Б. Мовчан и А. Демчишин: "Исследования структуры и свойств толстых вакуумных конденсатов никеля, титана, вольфрама, окиси алюминия и двуокиси циркония" <<Физика металлов и металловедение>> **28** [4] (1969) 23-30 (653 – 660 in transliterated version – Fizika Metallov i Metallovedeniye)}
- [98] J. Thornton: "High rate thick film growth" *Annual Reviews in Materials Science* **7** (1977) 239 – 60
- [99] P. Barna and M. Adamik: "Fundamental structure forming phenomena of polycrystalline films and the structure zone models" *Thin Solid Films* **317** (1998) 27 – 33
- [100] I. Petrov, P. Barna, L. Hultman and J. Greene: "Microstructural evolution during film growth" *Journal of Vacuum Science and Technology A* **21** [5] (2003) S117 – 28
- [101] E. Bauer: "Growth of oriented films on amorphous surfaces", *Single-Crystal Films* M. Francombe, H. Sato [Eds], Pergamon Press, Oxford UK (1964) ISBN B000H9YU78
- [102] J. Das, M. Tang, K. Kim, R. Theissmann, F. Baier, W. Wang and J. Eckert: "'Work-hardenable' ductile bulk metallic glass" *Physical Review Letters* **94** [20] (2005) 205501

-
- [103] J. Chang, Y.-S. Lin and K. Chu: "Rapid thermal chemical vapor deposition of zirconium oxide for metal-oxide-semiconductor field effect transistor application" *Journal of Vacuum Science and Technology B* **19** [5] (2001) 1782 – 7
- [104] J. Zhang, Z.-L. Wang, J. Liu, S. Chen, G.-Y. Liu: *Self Assembled Nanostructures*, Kluwer Academic Publishers, New York (2003) ISBN 0-306-47941-9
- [105] C. Brundle, C. Evans Jr. and S. Wilson: *Encyclopedia of Materials Characterization*, Butterworth-Heinemann, Stoneham MA, USA (1992) ISBN 0-7506-9168-9
- [106] N. Ashcroft and N. Mermin: *Solid State Physics*, Harcourt Inc., Orlando, FL, USA (1976) ISBN: 0-03-083993-9
- [107] W. Marra, P. Eisenberger and A. Cho: "X-ray total-external-reflection–Bragg diffraction: A structural study of the GaAs–Al interface" *Journal of Applied Physics*, **50** [11] (1979) 6927 – 33
- [108] A. Segmüller: "Characterization of epitaxial thin films by X-ray diffraction" *Journal of Vacuum Science and Technology A* **9** [4] (1991) 2477 – 82
- [109] P. Scardi, M. Leoni and M. D’Incau: "X-ray analysis of texture domains in nonhomogeneous thin films deposited by physical vapour deposition" *Thin Solid Films* **467** (2004) 326 – 33
- [110] D. Williams and C. Carter: *Transmission Electron Microscopy: A Textbook for Materials Science* Plenum Press, New York USA (1996) ISBN 0-306-45324-X
- [111] P. Persson: "Transmission electron microscopy" Course Presentation, Electron Microscopy, Linköpings universitet (2006)
- [112] P. Flewitt and R. Wild: *Physical Methods for Materials Characterisation, 2nd Edition* IOP Publishing Ltd. Bristol UK (2003) ISBN: 0-7503-0808-7
- [113] P. Persson: "Characterization of process-related defects in silicon carbide by electron microscopy" PhD Thesis, Linköpings universitet, Sweden (2001), ISBN 91-7373-039-4
- [114] M. O’Keefe, P. Buseck and S. Ijima: "Computed crystal structure images for high resolution electron microscopy" *Nature* **274** (1978) 322 – 4
- [115] M. O’Keefe. "Simulated HRTEM images of rotating nano-size metal particles", *Proceedings of the International Conference on Electron Microscopy* **14** [1] (1998) 163 – 4
- [116] D. Foord, B. Freitag, C. Kübel and D. Tang: "Tecnai advanced materials science" FEI Applications Laboratory, Eindhoven, The Netherlands (2002)
- [117] J. Hutchison: "Advanced techniques for high resolution electron microscopy", RMS Spring School (2006)
- [118] *Introduction to Analytical Electron Microscopy* J. Hren, J. Goldstein and D. Joy [Eds.], Plenum Press, New York, USA (1979) ISBN 0-306-40280-7
- [119] R. Egerton: *Electron Energy-Loss Spectroscopy In The Electron Microscope*, Plenum Press, New York (1996) ISBN 0-306-45223-5
- [120] R. Brydson: *Electron Energy Loss Spectroscopy*, BIOS Scientific Publishers, London, UK (2001) ISBN: 1-85996-134-7
- [121] R. Brydson: "Electron energy loss spectroscopy in electron microscopy: General principles" RMS Spring School (2006)
- [122] A. Bleloch: "Scanning transmission electron microscopy", RMS Spring School (2006)
- [123] *Ion Beams for Materials Analysis*, J. Bird and J. Williams [Eds.], Academic Press, Sydney, Australia (1989) ISBN 0-12-099740-1
- [124] T. Seppänen: "Growth and characterization of metastable wide band-gap Al_{1-x}In_xN epilayers" PhD Thesis, Linköpings universitet, Sweden (2006) ISBN 91-85523-58-5
- [125] H. Andersen and J. Zeigler: *The Stopping Powers and Ranges in All Elements*, Pergamon, New York, USA (1977) ISBN 0080216056
- [126] J. Hudson: *Surface Science – An Introduction*, Butterworth-Heinemann, Boston, USA (1992) ISBN 0-7506-9159-X
- [127] *Practical Surface Analysis – Volume I – Auger and X-Ray Photoelectron Spectroscopy*, 2nd Edition, D. Briggs and M. Sheah [Eds.], John Wiley & Sons, New York (1990) ISBN 0-471-95340-7
- [128] M. Seah: "A system for the intensity calibration of electron spectrometers" *Journal of Electron Spectroscopy and Related Phenomena* **71** (1995) 191 – 204
-

Populärvetenskaplig sammanfattning

”Nanocrystalline Alumina-Zirconia

Thin Films by Magnetron Sputtering”

David Huy Trinh

Institution för fysik, kemi och biologi (IFM)

Dagens materialforskning är fokuserad mot utveckling av avancerade material med skräddarsydda egenskaper. Genom att kontrollera ett materials uppbyggnad på nanometerskalan (miljondels millimeter) ges nya möjligheter att växa material som är exempelvis energisnålare, fungerar vid högre temperaturer eller har högre korrosionsmotstånd än befintliga material. Tillverkning av sådana material kräver dock precisa tillväxtförhållanden med avseende på materialflöde, temperatur, tryck o.s.v. för att styra materialets sammansättning och struktur. Här har material växta som tunna filmer visat sig särskilt lovande. Med tunnfilmsteknik beläggs ett basmaterial, så kallat substrat, med en film med tjocklek som varierar från ett atomlager, till en tusendels milimeter. Filmens egenskaper skräddarsys för en viss funktion, medan basmaterialet ger form och mekanisk hållfasthet.

I den här avhandlingen har tunnfilmstillväxt av två teknologiskt viktiga keramiska material, aluminiumoxid och zirkoniumoxid studerats. En tillämpning för filmerna är inom skärande bearbetning. Här är aluminiumoxidfilmer i dag dominerande, givet sin höga motståndskraft mot kemiska angrepp, höga hållfasthet och slitstyrka vid höga temperaturer. Ett tillkortakommande i sådana tillämpningar är dock aluminiumoxids låga brottseghet, vilket leder till skiktförstöring. Syftet med arbetet har varit att förbättra redan goda egenskaper genom att på nanometernivå designa skikt innehållande de båda keramerna, så kallade nanokompositer. Tendensen till sprickbildning i aluminiumoxid kan minskas genom att blanda i zirkoniumoxid och på så sätt få ett mer brottsegt material. Förbättringen är dock beroende på vilken fas av zirkoniumoxid som används, där de största fördelarna inte fås med den stabila monoklina fasen utan med den tetragonala fasen. Den senare kräver stabilisering med andra oxider typiskt från sällsynta jordartsmetaller såsom yttrium och cerium. Det har visat sig svårt från vanliga tillverkningstekniker att framställa och bibehålla andra faser förutom den stabila, vilket beror på de höga temperaturer och tryck som är nödvändiga under materialsyntesen. I detta arbete har en teknik som kallas för PVD (Physical Vapour Deposition) använts, mera specifikt magnetronsputtring. Principen är att energirika joner i ett plasma, typiskt en joniserad ädelgas som argon, bombarderar ytan av ett källmaterial. Kollisionen mellan jonerna i plasmat och atomerna i källan gör att ytomerna lösgörs från källan och transporteras bort i form av en ånga. Processen har slående likheter med första sprängningen i en biljardmatch där objektbollarna (de nummerade kloten) får representera materialkällan, emedan köbollen utgör den energirika jonen. Den transporterade ångan av högenergetiska atomer kondenserar slutligen mot substratets yta för att skapa en fast film. Under denna process kommer energin från atomerna att överföras till substratets yta. Detta skapar tillväxtförhållanden långt från termisk jämvikt och gör extern uppvärmning av substratet i det närmaste överflödig. PVD- och sputtringprocesser kan därför utföras

vid relativt låga temperaturer, vilket möjliggör syntes av strukturer där atomerna intar positioner som de normalt inte har vid förhållanden av normal temperatur och tryck. Dessa är så kallade metastabila faser varav den tetraonkala zirkoniumoxidfasen är ett exempel. Vidare är lågtemperaturprocesser fördelaktiga vid beläggning av exempelvis värmekänsliga basmaterial. På det hela taget erbjuder således PVD-tekniken uttalade fördelar vid tillväxt av framtidens tillämpningsdesignade material.

Studierna presenterade i denna avhandling visar att nanokompositer med metastabila faser är möjliga vid temperaturer inom området 300-800°C. Med tre studier har författaren visat att olika metastabila faser kan växas i nanokompositform vid en mängd olika beläggningsbetingelser. Djuplodande analyser med högupplösande elektronmikroskopi visar att de växta nanokompositfilmerna består av 10-20 nanometer stora kristaller av zirkoniumoxid, vilka omsluts av en nanometertjock hinna av huvudsakligen amorf aluminiumoxid. En sådan designad struktur på nanometerskalan är lovande för utsikterna att ytterligare förbättra egenskaperna jämfört med enskilda oxider. Förutom tillväxt av nanokompositfilmer omfattar avhandlingen också ett arbete där transportfasen av sputtrat material genom plasmata studeras. Ett viktigt resultat är att sammansättningen av sputterången och därigenom fasinnehållet hos filmen kan kopplas till parametrar i sputtringprocessen, t.ex. typen av kraftaggregat som driver sputtringsprocessen, eller om det finns en reaktiv gas i närvaro i plasmata. Detta visar på vikten av att studera processen i alla dess aspekter, d.v.s. från skapandet av sputterången via transporten av sputtrat material och slutligen kondensationen av ången. Med den motivationen har ett arbete inriktats mot att vidareutveckla en teoretisk modell gällande transport under sputterprocessen. Resultaten från studien visar på stor överensstämmelse mellan modell och experimentella observationer; framförallt gällande filmernas sammansättning, men även också sputterprocessens stabilitet. Genom att studera kombinationen av tillverkningsprocessen och materialet har författaren visat att design av material med bättre egenskaper är möjligt inom aluminiumoxid-zirkoniumoxid-materialsystemet.